

Deep learning to achieve clinically applicable segmentation of head and neck anatomy for radiotherapy

Stanislav Nikolov^{1*}, Sam Blackwell^{1*}, Ruheena Mendes², Jeffrey De Fauw¹, Clemens Meyer¹, Cian Hughes¹, Harry Askham¹, Bernardino Romera-Paredes¹, Alan Karthikesalingam¹, Carlton Chu¹, Dawn Carnell², Cheng Boon³, Derek D'Souza², Syed Ali Moinuddin², Kevin Sullivan², DeepMind Radiographer Consortium¹, Hugh Montgomery^{2,4,5}, Geraint Rees^{2,4}, Ricky A. Sharma^{2,4}, Mustafa Suleyman¹, Trevor Back¹, Joseph R. Ledsam¹⁺, and Olaf Ronneberger¹⁺

¹DeepMind, London, UK

²University College London Hospitals NHS Foundation Trust, London, UK

³Worcester NHS Foundation Trust, Worcester, UK

⁴University College London, London, UK

⁵Centre for Human Health and Performance, and Institute for Sports, Exercise and Health, University College London, London, UK

*These authors contributed equally to this work

+These authors contributed equally to this work

Over half a million individuals are diagnosed with head and neck cancer each year worldwide. Radiotherapy is an important curative treatment for this disease, but it requires manually intensive delineation of radiosensitive organs at risk (OARs). This planning process can delay treatment commencement. While auto-segmentation algorithms offer a potentially time-saving solution, the challenges in defining, quantifying and achieving expert performance remain. Adopting a deep learning approach, we demonstrate a 3D U-Net architecture that achieves performance similar to experts in delineating a wide range of head and neck OARs. The model was trained on a dataset of 663 deidentified computed tomography (CT) scans acquired in routine clinical practice and segmented according to consensus OAR definitions. We demonstrate its generalisability through application to an independent test set of 24 CT scans available from The Cancer Imaging Archive collected at multiple international sites previously unseen to the model, each segmented by two independent experts and consisting of 21 OARs commonly segmented in clinical practice. With appropriate validation studies and regulatory approvals, this system could improve the effectiveness of radiotherapy pathways.

1 Introduction

Each year, 550,000 people are diagnosed with cancer of the head and neck worldwide [1]. This incidence is rising [2], more than doubling in certain subgroups over the last 30 years [3, 4, 5]. Where available,

most will be treated with radiotherapy which targets the tumour mass and areas at high risk of microscopic tumour spread. However, normal anatomical structures ('organs at risk', OARs) may also be irradiated, with the dose received being directly correlated with adverse symptoms suffered [6, 7, 8]. Strategies to reduce incidental OAR dosing can reduce the side effects incurred [9].

The efficacy and safety of head and neck radiotherapy requires accurate OAR and tumour segmentation. However, the results of this process can be both inconsistent and imperfect in accuracy [10]. It is predominantly done manually, and so is dependent on the high-level expertise and consistent performance of the individuals performing the task. Unsurprisingly, large inter- and intra-practitioner variability exists, which can create challenges for the quality assurance of dosimetric impact on OARs [11]. Segmentation is also very time consuming: an expert can spend four hours or more on a single case [12]. This can cause clinically significant delays to treatment commencement (see Fig. 1); the duration of this delay is associated with increased risk of both local recurrence and overall mortality [13, 14]. Notably, the rising incidence of head and neck cancers [4] is driving demand for experts which might ultimately be hard to meet. Indeed, increasing demands for and shortages of trained staff already place a heavy burden on healthcare systems, which can lead to long delays for patients as radiotherapy is planned [15, 16]. Such pressures also present a barrier to the implementation of "Adaptive Radiotherapy", in which radiotherapy would be adapted to anatomic changes (such as tumour shrinkage) during treatment, preventing healthy tissue being exposed to greater radiation doses than necessary [17]. This unnecessary exposure could be avoided if OARs could be re-segmented at sufficiently regular intervals during a course of radiotherapy.

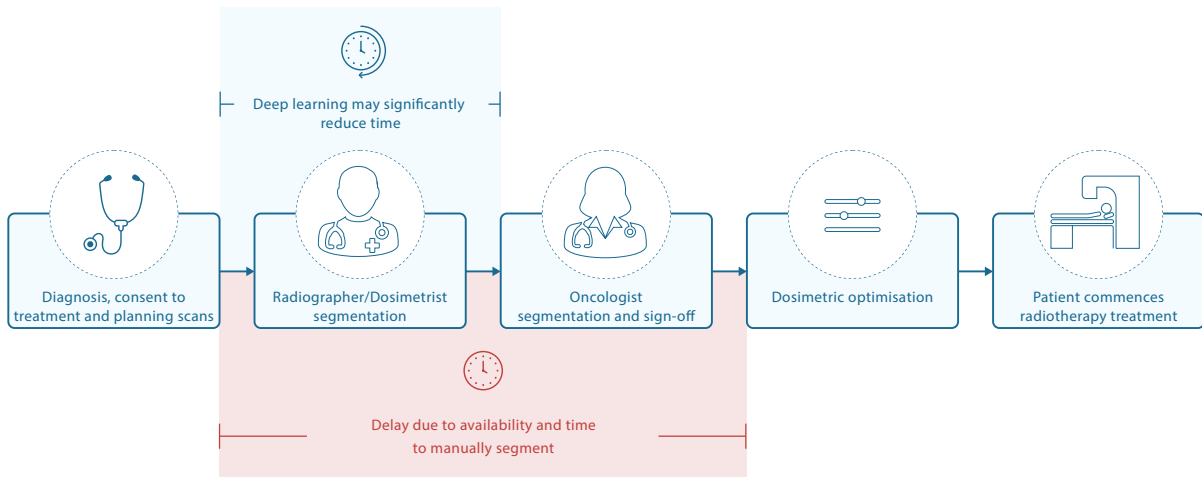


Figure 1 | A typical clinical pathway for radiotherapy. After a patient is diagnosed and the decision is made to treat with radiotherapy, a defined workflow aims to provide treatment that is both safe and effective; in the UK the time delay between decision to treat and treatment delivery should be no greater than 31 days. The manual segmentation and dose optimisation steps are manually intensive, and introduce potential delays to patients receiving treatment. Our work aims to reduce delays in manual segmentation (highlighted below in red) by evaluating deep learning in the first manual segmentation step (highlighted above). Note that in some centres OARs may be segmented by oncologists instead of therapeutic radiographers.

Automated (i.e. computer-performed) segmentation has the potential to address these challenges but, to date, performance of available solutions in clinical practice has proven inferior to that of expert human operators. Most segmentation algorithms in clinical use are atlas-based, producing their segmentations by extrapolating from manually labelled training examples. These algorithms might not sufficiently account for the variability in normal anatomical structure which exists between patients, particularly when considering the effect different tumours may have on local anatomy; thus these may be prone to systematic error. They perform at expert levels on only a small number of organs and the segmentations require

significant editing by human experts. Thus, they have failed to significantly improve clinical workflows [18, 19, 20, 21, 22, 23, 24, 25, 26, 27].

In recent years, deep learning based algorithms have proven capable of delivering substantially better performance than traditional segmentation algorithms. In particular the U-Net convolutional architecture [28] has shown promise in the area of deep-learning based medical image segmentation (see, e.g. [29]). In head and neck cancer segmentation, several deep learning based approaches have been proposed. Some of them use standard classification networks on patches [30, 31, 32, 33] with tailored pre- and post-processing, while others also use U-Net based architectures [34, 35, 36].

Despite the promise deep learning offers, challenges remain in developing clinical applicable algorithms. In particular the definition of 'expert' performance for a radiotherapy use case, unbiased quantification of this compared with human experts and subsequently achieving this present barriers to the application of auto-segmentation in radiotherapy treatment planning.

Here we address these challenges with a deep learning approach that performs at a standard similar to human experts in delineating a wide range of important OARs from radiotherapy scans for head and neck cancer. We achieve this by using a study design that includes (i) the introduction of a clinically-meaningful performance metric for segmentation in radiotherapy planning; (ii) a representative set of images and an independent test set from a site previously unseen to the model; (iii) an unambiguous segmentation protocol for all organs; and (iv) a segmentation of each test set image according to these protocols by two independent experts. By achieving performance similar to experts on a new and previously unseen group of patients we demonstrate the generalisability, and thus clinical applicability, of our approach.

2 Results

2.1 Datasets

We collated a representative sample of Computed Tomography (CT) scans used to plan curative-intent radiotherapy of head and neck cancer patients at University College London Hospitals NHS Foundation Trust (UCLH). To demonstrate the generalisability of models, we curated a test and validation set of open source CT scans available from The Cancer Imaging Archive ("TCIA test set") [37, 38, 39]. **Table 1** details the characteristics of these datasets and the patient demographics. Twenty-one organs at risk were selected to represent a wide range of anatomical regions throughout the head and neck; to account for human variability each case was segmented by a single radiographer with a second arbitrating and compared with a ground truth from two further radiographers arbitrated by one of two independent specialist oncologists. For more information on dataset selection, inclusion and exclusion criteria for patients and OARs please refer to the Methods section; further details are also described in a published protocol describing the collaboration with UCLH [40].

For the original volumetric segmentations received from UCLH, only those that meet quality and protocol conformity thresholds were included in the training data. Additional segmentations were added in the form of per-organ labelled axial slices to expand the training set while volumetric segmentations were added for OARs that consisted of fewer than ten slices. All training set segmentations were performed by experienced therapeutic radiographers¹ and went through a review and editing process with a second radiographer. Please refer to the Methods section for more details.

¹'Radiographer' is the term used to describe radiation therapy technologists in the United Kingdom and Australasia. Dosimetrists are other staff members that may be trained in manual segmentation. Oncologists are doctors specialising in the treatment of cancer. All oncologists involved in the reviewing and editing of manual segmentations for this study regularly plan radiotherapy treatment for head and neck patients as part of their routine clinical work.

Table 1 | Dataset Characteristics

		UCLH			TCIA		PDDCA
		Train	Validation	Test	Validation	Test	Test
Total scans (patients)		663 (389)	100 (51)	75 (46)	7 (6)	24 (24)	15 (15)
Average patient age		57.1	57.5	57.6	56.5	59.9	58.6
Gender	Female	207 (115)	36 (19)	18 (12)	2 (2)	2 (2)	2 (2)
	Male	450 (271)	64 (32)	57 (34)	5 (4)	20 (20)	9 (9)
	Unknown	6 (3)	0	0	0	2 (2)	4 (4)
Tumour site	Oropharynx	145 (86)	27 (15)	23 (11)	0	8 (8)	2 (2)
	Lip, oral cavity and pharynx	80 (52)	20 (8)	7 (6)	1 (1)	3 (3)	0
	Tongue	53 (26)	8 (5)	1 (1)	2 (2)	7 (7)	0
	Larynx	46 (31)	8 (3)	6 (4)	2 (2)	4 (4)	0
	Nasopharynx	48 (24)	5 (3)	1 (1)	0	0	0
	Head, face and neck	37 (23)	8 (3)	8 (4)	0	0	0
	Nasal Cavity	32 (19)	2 (1)	3 (2)	0	0	0
	Connective and soft tissue	37 (18)	2 (1)	5 (2)	0	0	0
	Hypopharynx	17 (10)	1 (1)	3 (2)	2 (1)	1 (1)	0
	Accessory sinus	10 (7)	2 (1)	0	0	0	0
	Oesophagus	6 (2)	1 (1)	1 (1)	0	0	0
	Other	33 (20)	0	1 (1)	0	1 (1)	0
	Unknown	119 (71)	16 (9)	16 (11)	0	0	13 (13)
Source	TCGA	-	-	-	2 (2)	7 (7)	0
	HN_Cetux	-	-	-	5 (4)	17 (17)	15 (15)
Site	UCLH	663 (389)	100 (51)	75 (46)	0	0	0
	MD Anderson Cancer Clinic	0	0	0	2 (2)	7 (7)	0
	Unknown (US)	0	0	0	5 (4)	17 (17)	15 (15)

Tumour sites are taken from ICD codes. Numbers show number of scans as well as numbers of unique patients in parenthesis.

"TCGA": The Cancer Genome Atlas Head-Neck Squamous Cell Carcinoma[39], an open source dataset hosted on TCIA.

"HN_Cetux": Head-Neck Cetuximab, an open source dataset hosted on TCIA[37]. "PDDCA": Public Domain Database for Computational Anatomy dataset released as part of the 2015 challenge in the segmentation of head and neck anatomy at the International Conference On Medical Image Computing & Computer Assisted Intervention (MICCAI).

2.2 Qualitative performance

We used a 3D U-Net architecture [28, 41] with similar design choices as in a study of De Fauw and colleagues [29] (see Fig. 7). At each resolution we use residual blocks [42] with a combination of padded xy-convolutions and unpadded z-convolutions. The unpadded convolutions allow very efficient training when the labelled slices are sparse within the scan and allow a seamless tiling [28, 41] of large volumes in the z-direction which is useful because the full volumes do not fit into the memory of the Graphics Processing Unit (GPU). In contrast to common semantic segmentation tasks our 21 segmentation labels are not mutually exclusive, i.e. a voxel can belong to multiple structures, like "spinal cord" and "spinal canal". In order to account for this the final layer of the network applies a (channel wise) sigmoid instead of a softmax. Network training is done on subvolumes determined by a central slice and the required context for that slice. To account for the class imbalance – the organ volumes range from around 65mm³ (cochlea) to around 1,400,000mm³ (brain) – we use a top-k loss [43] during training. The prediction is done in tiles in the z-direction. The model took on average less than 30 seconds on a single GPU to compute the 21 OAR predictions for each test set scan. For further details please refer to the Methods section.

Qualitative examples of the model's performance on a representative CT scan from the TCIA test set are shown in Fig. 2. Deep learning segmentations are shown against a ground truth defined by a consultant oncologist with over 10 years of experience in segmenting OARs. The levels shown as 2D slices have

been selected to demonstrate all 21 OARs included in this study.

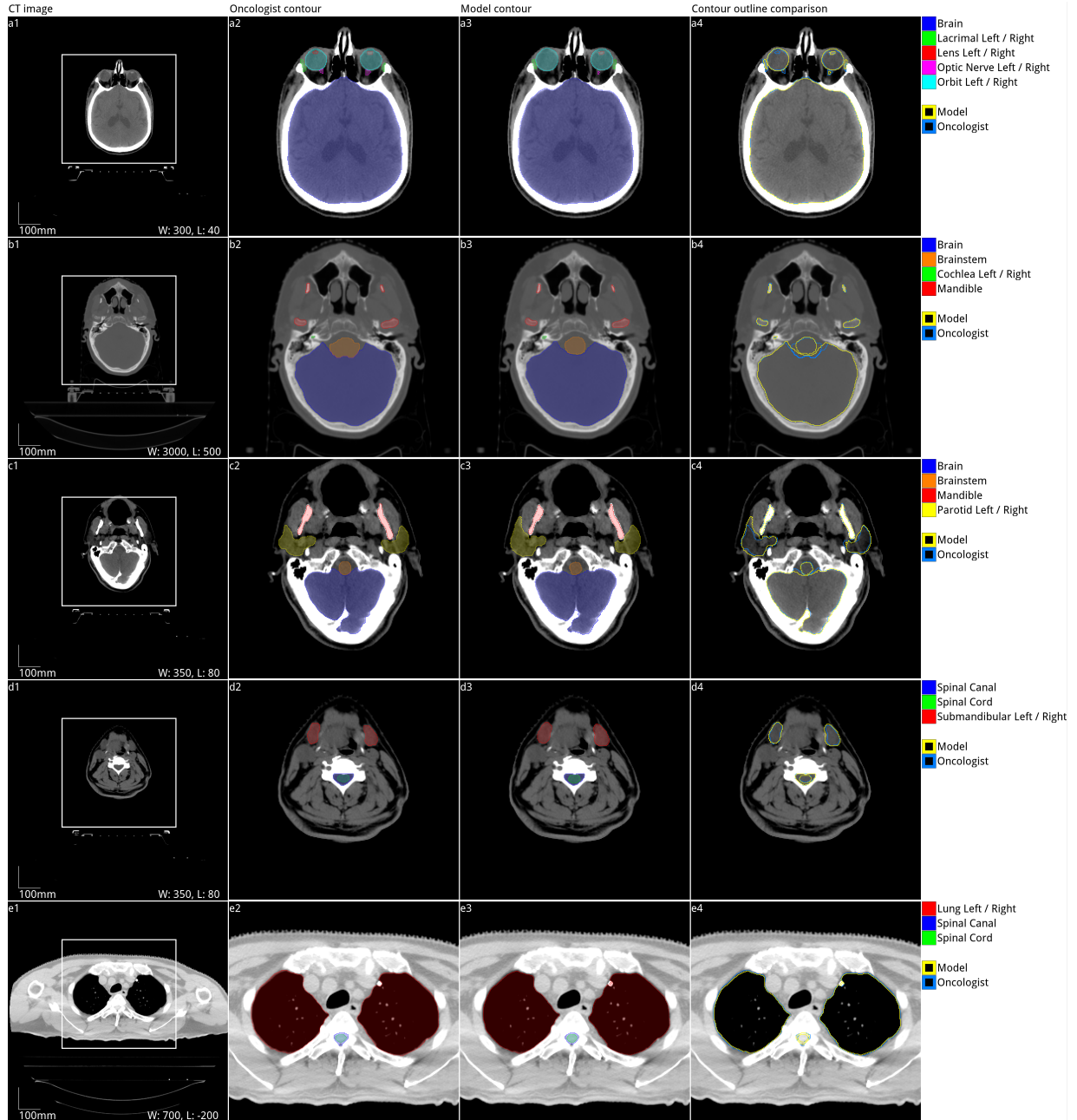


Figure 2 | Example results from a randomly selected case from the TCIA test set. Five axial slices from the scan of a 66 year old male patient with a right base of tongue cancer with bilateral lymph node involvement selected from the Head-Neck Cetuximab TCIA dataset (patient 0522c0057; [37]). (a1-e1) The raw CT scan slices at five representative levels were selected to best demonstrate the OARs included in the work. The window levelling has been adjusted for each to best display the anatomy present. (a2-e2) The ground truth segmentation was defined by experienced radiographers and arbitrated by a head and neck specialist oncologist. (a3-e3) Segmentations produced by our model. (a4-e4) Overlap between the model (yellow line) and the ground truth (blue line). Two further randomly selected TCIA set scans are shown in Fig. 11 and Fig. 12. Best viewed on a display.

2.3 Quantitative performance

For quantitative analysis we introduce a segmentation performance metric, "surface Dice-Sørensen Coefficient" (surface DSC), that is better suited for the presented use case than the standard volumetric Dice-Sørensen Coefficient (volumetric DSC; [44]) as it provides a measure of the agreement between just the surfaces of two structures.

In our use case, predicted segmentations would be reviewed and potentially corrected by a human expert, so we primarily care about the fraction of the surface that needs to be redrawn because it is too far from the ground truth surface (see Fig. 3). The volumetric DSC is not well suited for this because it weights all misplaced segmentation labels equally and independently of their distance from the surface. For example, a segmentation that violates the surface tolerance by a small amount at many places (requiring the time-consuming correction of large parts of the border) might still get a good volumetric DSC score. In contrast, another segmentation that violates the surface tolerance by a large degree but at a single place (which could be manually corrected with relative ease) might end up with a poor volumetric DSC score. Furthermore the volumetric DSC penalises the deviation from the ground truth relative to the organ's volume. In radiotherapy planning the absolute deviation (in mm) is important, independent of the organ's size, to ensure that radiation planning can be accurately and safely performed.

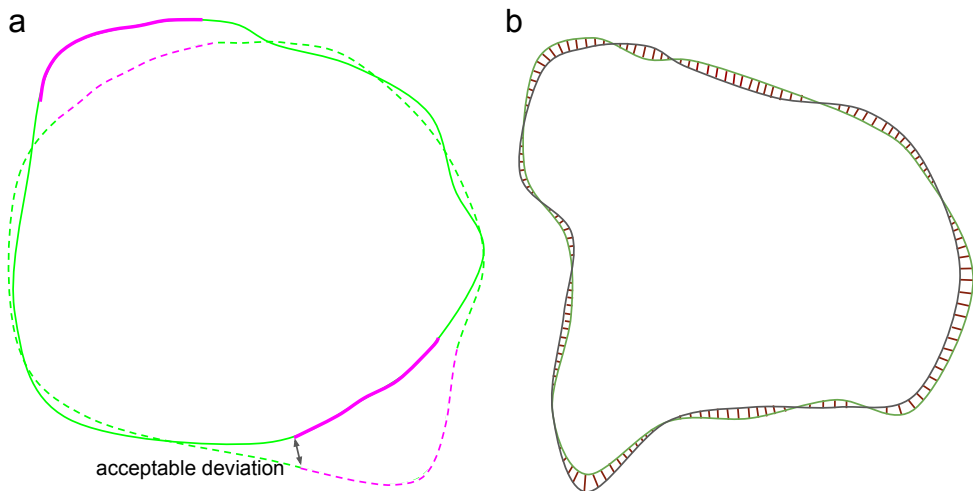


Figure 3 | Surface DSC performance metric. (a) Illustration of the computation of the surface DSC. Continuous line: predicted surface. Dashed line: ground truth surface. Black arrow: the maximum margin of deviation which may be tolerated without penalty, hereafter referred to by τ . Note that in our use case each OAR has an independently calculated value for τ . Green: acceptable surface parts (distance between surfaces $\leq \tau$). Pink: unacceptable regions of the surfaces (distance between surfaces $> \tau$). The proposed surface DSC metric reports the good surface parts compared to the total surface (sum of predicted surface area and ground truth surface area). (b) Illustration of the determination of the organ-specific tolerance. Green: segmentation of an organ by oncologist A. Black: segmentation by oncologist B. Red: distances between the surfaces. We defined the organ-specific tolerance as the 95th percentile of the distances collected across multiple segmentations from a subset of seven TCIA scans, where each segmentation was performed a radiographer arbitrated by an oncologist, neither of whom had seen the scan previously.

To evaluate the surface DSC we first defined organ-specific tolerances (in mm) as a parameter of the proposed metric. We computed these acceptable tolerances for each organ by measuring the inter-observer variation in segmentations between three different consultant oncologists (each with over 10 years of experience in clinical oncology delineating OARs) on a subset of our TCIA images. To penalise both false negative and false positive parts of the predicted surface our proposed metric uses the overlapping

area from both surfaces (the predicted surface and the ground truth surface) and normalises it by the total surface area (sum of predicted surface area and ground truth surface area). Like the volumetric DSC, the surface DSC ranges from 0 (no overlap) to 1 (perfect overlap). Put simply, a surface DSC of 0.95 means that approximately 95% of the surface was properly outlined (as defined by the acceptable tolerance parameter τ) while 5% needs to be corrected. For a more formal definition and implementation, please refer to the Methods section.

Model performance was evaluated alongside that of therapeutic radiographers (each with at least 4 years of experience) segmenting an independent test and validation set collected from an entirely different population than the training dataset. Each test set case was segmented by a single radiographer with a second arbitrating, and compared with a ground truth from two further radiographers arbitrated by one of two independent specialist oncologists.

The models performed similarly to humans: on 19 of 21 OARs there was no substantial difference between the deep learning models and that of the radiographers (Fig. 4 and Table 4). Given the variations of performance differences, we define a substantial difference here as 5% or more. The two exceptions were the brainstem and right lens, where our model’s performance was inferior to that of the human experts.

To understand the performance in clinical practice we computed an aggregated surface DSC per patient over only those organs that would currently be segmented given that patient’s tumour diagnosis. As different OARs have largely different sizes the aggregate surface DSC provides a better estimate of potential time saved for each patient. Here we first summed up the overlapping surface area as well as the total surface area of all relevant organs for the individual patient. We then computed the surface DSC (Table 4 last rows). We found that for all 24 patients there was no substantial difference between the models and the radiographers performance in any individual patient (Table 4 last row).

In addition to demonstrating a surface DSC score comparable to that of the radiographers’ we also report the standard volumetric DSC scores, despite its shortcomings for our described use case, to allow a qualitative comparison of our results to those in the existing literature. An accurate quantitative comparison to previously published literature is difficult due to inherent differences in the datasets used: performance may vary considerably across datasets and a meaningful comparison cannot be achieved without defining, and subsequently using, a consistent and precise protocol for how OARs should be segmented and obtaining results on the same dataset. For more detailed results demonstrating surface DSC and volumetric DSC for each individual patient from the TCIA test set please refer to Table 4 and Table 5 respectively in the appendix.

2.4 Comparison to previous work

Table 2 shows the results of a systematic review of relevant previous papers reporting mean volumetric DSC for the unedited automatic delineation of head and neck OARs from CT images. These are compared with our model’s performance on the TCIA open source test set, as well as an additional test set from the original UCLH dataset (“UCLH test set”) and the Public Domain Database for Computational Anatomy (PDDCA) dataset released as part of the 2015 MICCAI challenge in the segmentation of OARs for head and neck radiotherapy (“PDDCA test set”; [45]). To contextualise the performance of our model, radiographer performance is shown on the TCIA test set, and oncologist inter-observer variation is shown on the UCLH test set. Each study used different data sets, scanning parameters and labelling protocols and so the resulting volumetric DSC results vary significantly. No studies were identified that included lacrimal glands. While not used as the primary test set we nevertheless present both surface DSC and volumetric DSC for each individual PDDCA test set patient in Table 6 and Table 7 respectively in the appendix.

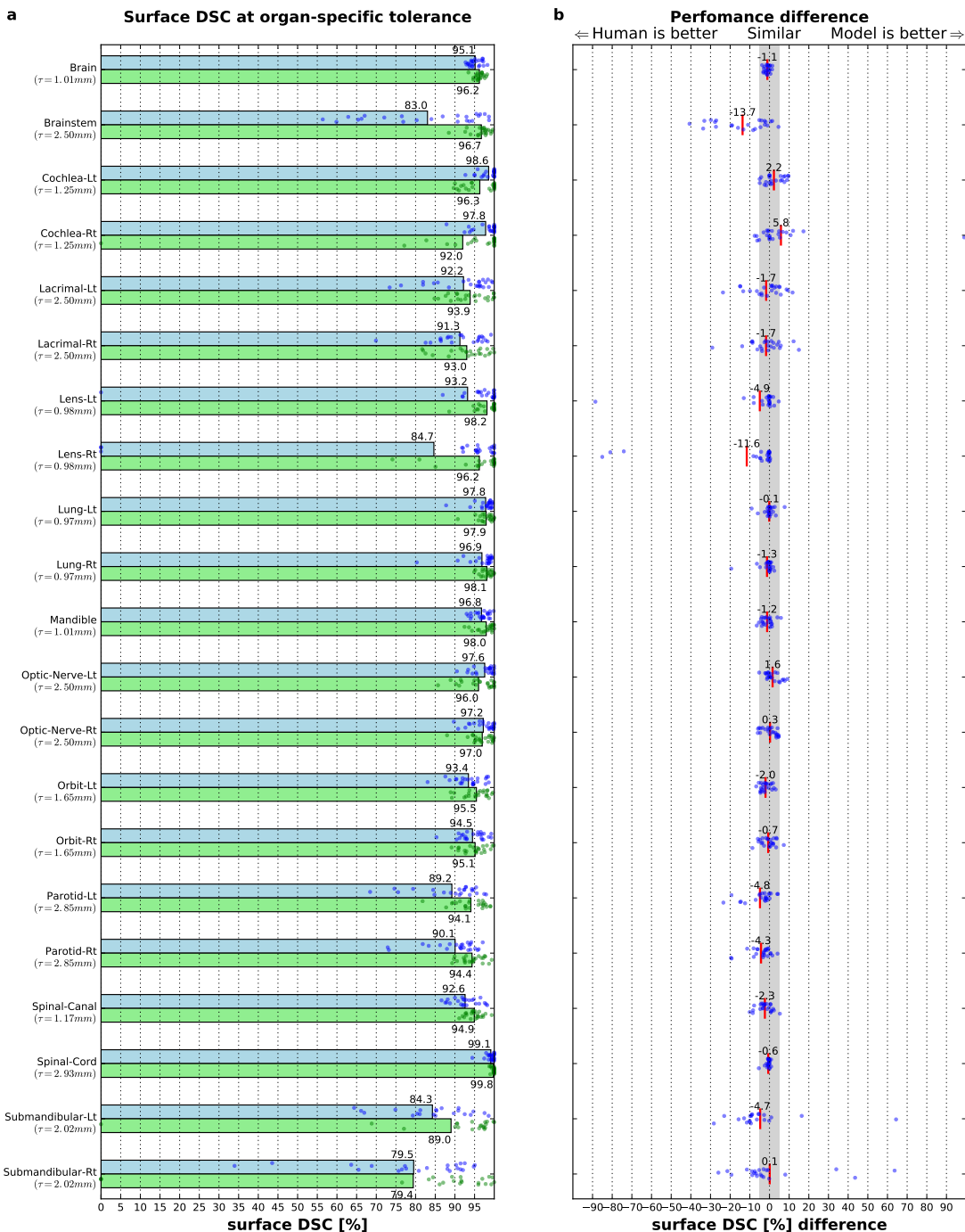


Figure 4 | Quantitative performance of the model in comparison to radiographers. (a) Surface DSC (on the TCIA open source test set) for the segmentations compared to the gold standard for each organ at an organ-specific tolerance τ . Bars show the mean value. Blue: our model, green: radiographers. (b) Performance difference between the model and the radiographers. Each blue dot represents a model-radiographer pair. Red lines show the mean difference. The grey area highlights non-substantial differences (-5% to +5%)

Table 2 | Volumetric DSC performance of our model and previously published results.

Study	Method	Brain	Brainstem	Cochlea		Lacrimal		Lens		Lung		Mandible	Optic Nerve	Orbit	Parotid	Spinal-Canal	Spinal-Cord	Submandibular				
				lt	rt	lt	rt	lt	rt	lt	rt	lt	rt	lt	rt	lt	rt	lt	rt			
Hoogeman (2008) [21]	Multi-ABAS		71 ¹															71 ¹				
Sims (2009) [24]	Multi-ABAS		77																			
Qazi (2011) [23]	HAS		91																			
Teguh (2011) [25]	Multi-ABAS		78 ¹																			
Daisne (2013) [18]	Single-ABAS		75 ²																			
Fortunati (2013) [19]	HAS		78																			
Thomson (2014) [26]	HAS																					
Hoang Duc (2015) [20]	Multi-ABAS		83 ²																			
Walker (2015) [27]	HAS		97																			
Fritscher (2016) [30]	Deep learning																					
Ibragimov (2017) [31]	Deep learning																					
Raudashl (2017) [45]	HAS																					
Hänsch (2018) [34]	Deep learning																					
Močnik (2018) [32]	Deep learning																					
Ren (2018) [33]	Deep learning																					
Tam (2018) [46]	Machine learning	91		67	72			75	74			85		94	94	83	82	83	87			
Wang (2018) [47]	Machine learning											94		82	83							
Zhu (2018) [35]	Deep learning											93		72	71	88	87	81	81			
Tong (2018) [36]	Deep learning											94		65	69	84	83	76	81			
Radiographer (TCIA) (24 scans)	Manual	99.1 ¹ ±0.3	89.5 ±2.2	77.9 ±8.0	72.0 ±20.3	65.6 ±10.3	66.5 ±10.4	87.2 ±8.3	83.4 ±15.6	98.7 ±0.7	98.8 ±0.5	93.9 ±2.3	78.8 ±5.0	77.6 ±6.4	92.9 ±1.9	93.0 ±1.7	86.7 ±3.5	87.0 ±3.1	93.9 ±1.9	84.0 ±4.8	83.3 ±19.7	74.9 ±30.2
Our model (TCIA) (24 scans)	Deep Learning	99.0 ±0.2	79.1 ±9.6	81.8 ±6.7	80.8 ±7.8	61.8 ±12.9	60.6 ±10.8	80.0 ±18.4	73.1 ±28.2	98.8 ±0.6	98.6 ±1.0	93.8 ±1.6	78.1 ±5.1	77.0 ±5.0	91.5 ±2.1	92.1 ±1.9	83.2 ±5.4	84.0 ±3.7	92.3 ±1.8	80.0 ±7.8	80.3 ±7.8	76.0 ±16.5
Oncologist (UCLH) (8 - 75 scans) ⁴	Manual	99.0 ⁵	91.9 ⁵	68.5 ±14.8	75.8 ±8.5	63.3 ±13.1	61.6 ±14.3	86.2 ±10.1	87.6 ±9.9	98.4 ⁵ ±9.9	98.6 ⁵	95.4 ⁵	77.1 ±6.3	76.0 ±7.1	94.8 ⁵ ±7.1	94.8 ⁵ ±7.1	90.1 ⁵ ±7.1	90.7 ⁵	94.9 ⁵	87.7 ⁵	91.1 ⁵	90.1 ⁵
Our model (UCLH) (8 - 75 scans) ⁴	Deep Learning	99.1 ⁵	87.6 ⁵	65.2 ±15.3	74.9 ±10.0	69.1 ±11.5	69.6 ±11.7	80.6 ±11.6	80.0 ±11.6	98.7 ⁵ ±11.6	98.8 ⁵	95.7 ⁵	76.0 ±5.8	77.2 ±6.1	95.1 ⁵ ±6.1	94.8 ⁵ ±6.1	85.3 ⁵ ±6.1	84.9 ⁵	95.0 ⁵	88.1 ⁵	85.4 ⁵	84.8 ⁵
Our model (PDDCA) (15 scans)	Deep Learning		79.5 ±7.8									94.0 ±2.0	71.6 ±5.8	69.7 ±7.1		86.7 ±2.8	85.3 ±6.2		76.0 ±8.9	77.9 ±7.4		

Values for volumetric DCS are mean (\pm standard deviation) unless otherwise stated. "ABAS": atlas based auto segmentation.

"HAS": hybrid atlas-based segmentation.

¹ merged brainstem and spinal cord.

² Values estimated from figures; actual values not reported.

³ Median; mean not reported.

⁴ Number of scans per organ varies, see Table 8.

⁵ Volumetric DSC estimated from sparse labels.

3 Discussion

3.1 Model performance

We demonstrate an automated deep learning-based segmentation algorithm that can perform to a similar standard as experienced radiographers across a wide range of important OARs for head and neck radiotherapy. The final model performance in all regions except brainstem and right lens was similar to radiographers when compared to a gold standard of an expert consultant oncologist with over 10 years experience in treating patients with head and neck cancer. Our system was developed using CT scans derived from routine clinical practice with a test and validation set consisting of a new population collected from several different radiotherapy planning datasets, demonstrating the generalisability of an approach that should be applicable in a hospital setting for segmentation of OARs, routine Radiation Therapy Quality Assurance (RTQA) peer review and reducing the associated variability between different radiotherapy centres [48].

For 19 of the 21 OARs studied, our model achieved near expert radiographer level performance on the TCIA test set of scans taken from a previously unseen open source dataset. In brainstem and right lens the model's surface DSC score deviated by more than 5% from the radiographer performance, although the volumetric DSC for lens was similar to state-of-art compared to previously published results. Several factors may have contributed to this impaired performance. For brainstem, which comprises the midbrain, pons and medulla oblongata, the deviation between the ground truth and model segmentations frequently

occurred in defining where the brainstem begins. Brouwer and colleagues [49] define the level at which the brain transitions to brainstem (midbrain) as being that which extends inferior from the lateral ventricles. This definition is somewhat imprecise and thus difficult for the models to learn, and may also be confounded by inconsistencies observed between ground truth labels in the training data. If implemented in clinical practice, brainstem segmentation may require an oncologist or radiographer to edit, although it is possible that a post processing step to smooth the transition level between brainstem and brain could resolve this issue. Significant variation was observed in the lens, with the right lens falling below the 5% error margin of radiographer performance on the TCIA test set. Potential explanations may be the difficulty of identifying its borders in routine practice on CT scans, and the 2.5mm slice thickness and partial voluming effects due to the small size of the lens. These factors are evident on inspection of the data: performance in the UCLH test set (where scan quality was more consistent) was within the threshold for radiographer performance, while in a number of cases in the TCIA test set the lens was particularly difficult to identify and the model failed to segment it entirely (Fig. 10). Clinically, lower accuracy in outlining the lens is less concerning: during treatment a patient is unlikely to maintain the same gaze direction as in the planning CT scan. For this reason, the generally accepted International Guidelines [49] recommend instead delineating anterior and posterior orbit, regions that were not present in the training dataset. Future work will address this limitation by developing models that delineate these regions instead of the lenses.

Performance may have been affected by biases in the TCIA test set, which was made up of open source scans from a range of different centres. In particular, the Head-Neck Cetuximab inclusion criteria selected for patients with advanced head and neck cancer. This could have introduced a bias in favour of the humans and against our system by providing a more difficult set of images with substantial differences to the dataset on which the model was trained. In addition, although we excluded scans that were not representative of those used in routine clinical practice, the overall quality varied considerably when compared to the training and validation sets that were collected at a single specialist centre with access to high quality CT scanners. This may help to explain poorer performance on the lens OAR, where scan quality can make the borders difficult to ascertain (Fig. 10).

A final potential source of error is variability in training data. While all of our internally created segmentation volumes were created to adhere to a defined protocol, interobserver variation may still have confounded the results. A notable example of this is where the retromandibular vein runs through the parotid gland. The protocol used includes the vein only when it is fully encapsulated by parotid tissue; identifying this could be dependent on variables such as image artefacts and strength of contrast enhancement. Such variation, along with differences in image quality and in the software used to create the segmentations, is not uncommon in the ground truth and reflects the variation that might be seen in clinical practice [10]. The resulting variation may limit model performance as it introduces deviations from a consistent protocol in the training set; despite this, the model still performed to human expert standards in the majority of OARs.

3.2 Surface DSC: a clinically applicable performance metric

In this work we introduce the surface DSC, a metric conceived to be sensitive to clinically significant errors in delineation of organs at risk. While segmenting OARs for radiotherapy, small deviations in border placement can have a potentially serious impact, increasing the risk of debilitating side effects for the patient. Misplacement by only a small offset may require the whole region to be redrawn and in such cases an automated segmentation algorithm may offer no time-savings at all. The volumetric DSC is relatively insensitive to such small changes for large organs as the absolute overlap is also large. Difficulties identifying the exact borders of smaller organs, often due to ambiguity in the imaging process, can result in large differences in volumetric DSC even if these differences are not clinically relevant in terms of their

effect on radiotherapy treatment. By strongly penalising border placement outside a tolerance derived from consultant oncologists, the surface DSC metric resolves these issues. Future work should investigate the extent to which the surface DSC correlates with the saved time for manual segmentation.

3.3 Comparison with previous work

At least 11 auto-contouring software solutions are currently available commercially, with varying claims regarding their potential to lower segmentation time during radiotherapy planning [50]. The principal factor in determining whether or not automatic segmentations are time-saving during the radiotherapy workflow is whether they produce segmentations which are acceptable to oncologists and whether they require extensive (i.e. time consuming) corrections. Ibragimov and colleagues [31] used convolutional neural networks (CNN) smoothed by a Markov Random Fields algorithm and published the most comprehensive analysis to date, reporting a wide variation in geometric accuracy. Although performance for OARs such as mandible and spinal cord was good (volumetric DSC 0.90 and 0.87 respectively), performance on OARs which lack easily distinguishable intensity features was notably worse than existing non-deep learning algorithms (see Table 2 for more details on this and other prior publications). Indeed, there is considerable variation in the volumetric DSC reported in prior work. Although not directly comparable due to different datasets and labelling protocols, we present volumetric DSC results that compare favourably against the existing published literature for many of the OARs. Furthermore we present these results on three separate test sets, two of which (the TCIA and the PDDCA test sets) use different segmentation protocols. In those where the volumetric DSC score is higher in the published literature both our model and the human radiographers achieved similar scores, suggesting that current and previous results are particularly incomparable – either due to including more difficult cases than previous studies or due to the differences we have mentioned above. To allow more objective comparisons of different segmentation methods, we make our labelled TCIA datasets freely available to the academic community.²

Several studies have improved on the state-of-art results for OARs in CT scans released as part of the 2015 MICCAI Challenge in Head & Neck segmentation [45]. The challenge organisers added ground truth segmentations to selected scans from the Head-Neck Cetuximab TCIA dataset (one of the two open source datasets from which we selected our TCIA test set, though there was only a single scan present in both respective test sets). Scans in the MICCAI challenge set differ from our TCIA test set both in segmentation protocol and axial slice thickness. To further demonstrate the generalisability of our approach we present our volumetric DSC results on this dataset also (PDDCA test set, Table 2). Despite these differences, and without including any of their segmentations in our training data, our performance is still comparable to state-of-art for all organs except for brainstem (see previous discussion).

3.4 Limitations

The wide variability in state-of-art and limited uptake in routine clinical practice motivates the need for clinical studies evaluating model performance in practice. Future work will seek to define the clinical acceptability of the segmented OARs produced by our models, and estimating the time-saving which could be achieved during the radiotherapy planning workflow.

A number of other study limitations should also be addressed in future work. We included only planning CT scans since magnetic resonance imaging (MRI) and Positron Emission Tomography (PET) scans were not routinely performed for all patients in the UCLH dataset. Some OAR classes, such as optic chiasm, require co-registration with MRI images for optimal delineation and access to additional imaging has been shown to improve the delineation of optic nerves [32]. As a result certain OAR classes were deliberately excluded from this CT-based project and will be addressed in future work including MRI scans. With

²The dataset is available at <https://github.com/deepmind/tcia-ct-scan-dataset>.

regard to the classes of OARs in this study we present a larger set of OARs than previously reported [18, 19, 20, 21, 22, 23, 24, 25, 26, 27, 45, 30, 31, 34, 33, 46, 47, 35] but there are some omissions (e.g., oral cavity) as there were not a sufficient number of examples in the training data that conformed to a standard international protocol. The number of oncologists used in the creation of our ground truth may not have fully captured the variability in OAR segmentation, or may have been biased towards a particular interpretation of the Brouwer Atlas used as our segmentation protocol. Even in an organ as simple as the spinal cord that is traditionally done well by autosegmentation algorithms there is ambiguity between the inclusion of, for example, the nerve roots. Such variation may widen the thresholds of acceptable deviation in favour of the model despite a consistent protocol. Future work will address these deficits, alongside lymph node regions which represent another time consuming aspect of OAR outlining during radiotherapy planning.

3.5 Conclusion

In conclusion, we demonstrate that deep learning can achieve near human performance in the segmentation of a head and neck OARs on radiotherapy planning CT scans using a clinically applicable performance metric designed for this clinical scenario. We provide evidence of the generalisability of this model by testing it on patients from entirely different demographics. This segmentation algorithm can be used with very little loss in accuracy compared to an expert and has the potential to improve the speed and efficiency of radiotherapy workflows, therefore positively influencing patient outcomes. Future work will investigate the impact of our segmentation algorithm in clinical practice.

4 Methods

4.1 Datasets

University College London Hospitals NHS Foundation Trust (UCLH) serves an urban, mixed socioeconomic and ethnicity population in central London, U.K. and houses a specialist centre for cancer treatment. Data were selected from a retrospective cohort of all adult (>18 years of age) UCLH patients who had computed tomography (CT) scans to plan radical radiotherapy treatment for head and neck cancer between 01/01/2008 and 20/03/2016. Both initial CT images and re-scans were included. Patients with all tumour types, stages and histological grades were considered for inclusion, so long as their CT scans were available in digital form and of sufficient diagnostic quality. The standard CT element size was 0.976mm by 0.976mm by 2.5mm, and scans with non-standard spacing (with the exception of 1.25mm spacing scans which were subsampled) were excluded to ensure consistent performance metrics during training (note that for the TCIA test set, below, neither element height nor width were exclusion criteria and each ranged from 0.94mm - 1.27mm and were always equal to form square pixels in the axial plane. For the PDDCA test set we included all scans, and the voxels varied between 2mm and 3mm in height and ranged similarly in the axial dimension from 0.98mm - 1.27mm). The wishes of patients who had requested that their data should not be shared for research were respected.

Of the 513 patients who underwent radiotherapy at UCLH within the given study dates a total of 486 patients (838 scans), mean age 57, male 337, female 146, gender unknown 3, met the inclusion criteria. Of note, no scans were excluded on the basis of poor diagnostic quality. Scans from UCLH were split into a training set (389 patients, 663 scans), validation set (51 patients, 100 scans) and test set (46 patients, 75 scans). No patient was included in multiple datasets: in cases where multiple scans were present for a single patient, all were included in the same subset. Where multiple scans were present for a single patient this reflects planning CT scans taken for the purpose of re-planning radiotherapy due to anatomical changes during a course of treatment. While it is important for models to perform well in both scenarios

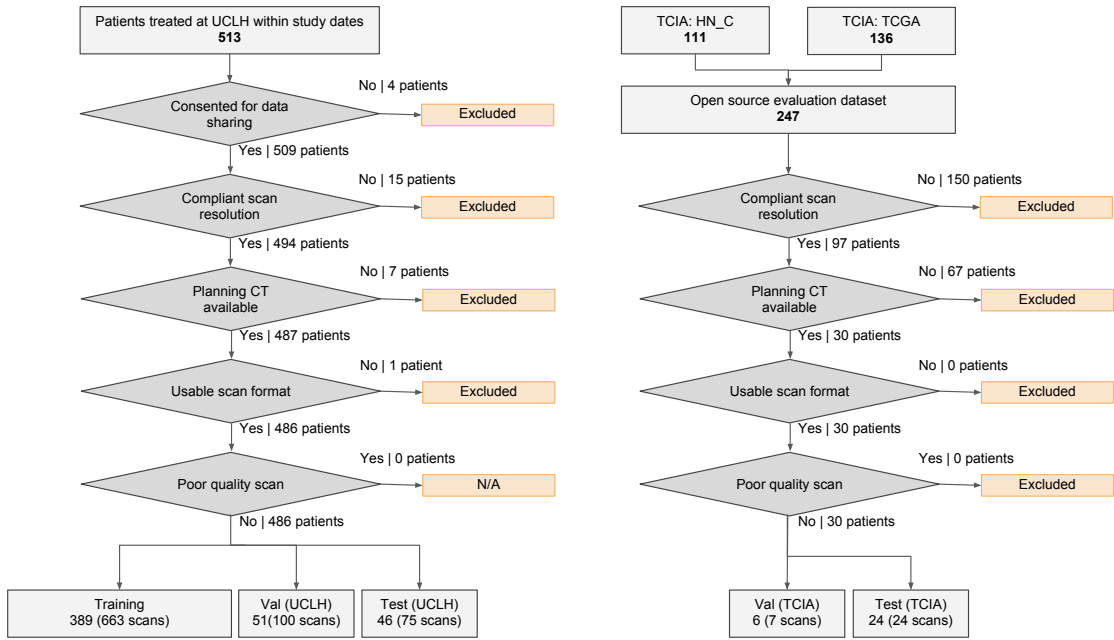


Figure 5 | Case selection from UCLH and TCIA CT datasets. A consort-style diagram demonstrating the application of inclusion and exclusion criteria to select the training, validation (val) and test sets used in this work.

as post operative OAR anatomy can differ from definite radiotherapy anatomy in important ways, to avoid potential correlation between the same organs segmented twice in the same dataset care was taken to avoid this in the TCIA test set (see below).

In order to assess the generalisability of the dataset, a separate validation and test set was curated from CT planning scans selected from two open source datasets available from The Cancer Imaging Archive [38]: TCGA-HNSC [39] and Head-Neck Cetuximab [37]. Non-CT planning scans and those that did not meet the same slice thickness as the UCLH scans (2.5mm) were excluded. These were then manually segmented in-house according to the Brouwer Atlas ([49]; the segmentation procedure is described in further detail below). We included 31 scans (22 Head-Neck Cetuximab, 9 TCGA-HNSC) which met these criteria, which we further split into validation (6 patients, 7 scans) and test (24 patients, 24 scans) sets (Fig. 5). The original segmentations from the Head-Neck Cetuximab dataset were not included; a consensus assessment by experienced radiographers and oncologists found the segmentations either non-conformant to the selected segmentation protocol or below the quality that would be acceptable for clinical care. The original inclusion criteria for Head-Neck Cetuximab were patients with stage III-IV carcinoma of the oropharynx, larynx, and hypopharynx, having Zubrod performance of 0-1, and meeting predefined blood chemistry criteria between 11/2005 to 03/2009. The TCGA-HNSC dataset included patients treated for Head-Neck Squamous Cell Carcinoma, with no further restrictions being apparent. For more information please refer to the specific citations [39, 37].

All test sets were kept separate during model training and selection, and only accessed for the final assessment of model performance, while the validation set was used only for model selection (see the Methods section for more details). Table 1 describes in further detail the demographics and characteristics within the datasets; to obtain a balanced demographic in each of the test, validation and training datasets

we sampled randomly stratified splits and selected one that minimised the differences between the key demographics in each dataset.

In addition the PDDCA open source dataset consisted of 15 patients selected from the Head-Neck Cetuximab open source dataset [37]; due to differences in selection criteria and test/validation/training set allocation there was only a single scan present in both the TCIA and PDDCA test sets. This dataset was used without further post-processing and only accessed once for assessing the volumetric DCS performance. For more details on the dataset characteristics and preprocessing please refer to the work of Raudaschl and colleagues [45].

4.2 Clinical taxonomy

In order to select which OARs to include in the study, we used the Brouwer Atlas (consensus guidelines for delineating OARs for head and neck radiotherapy, defined by an international panel of radiation oncologists; [49]). From this, we excluded those regions which required additional magnetic resonance imaging for segmentation, were not relevant to routine head and neck radiotherapy, or that were not used clinically at UCLH. This resulted in a set of 21 organs at risk; see [Table 3](#).

4.3 Clinical labelling & annotation

Due to the large variability of segmentation protocols used and annotation quality in the UCLH dataset, all segmentations from all scans selected for inclusion in the training set were manually reviewed by a radiographer with at least 4 years experience in the segmentation of head and neck OARs. Volumes that did not conform to the Brouwer Atlas were excluded from training. In order to increase the number of training examples, additional axial slices were randomly selected for further manual OAR segmentations to be added based on model performance or perceived imbalances in the dataset. These were then produced by a radiographer with at least 4 years experience in head and neck radiotherapy, arbitrated by a second radiographer with the same level of experience. The total number of examples from the original UCLH segmentations and the additional slices added are provided in [Table 3](#).

For the TCIA test and validation sets, the original dense segmentations were not used due to poor adherence to the chosen study protocol. To produce the ground truth labels the full volumes of all 21 OARs included in the study were segmented. This was done initially by a radiographer with at least four years experience in the segmentation of head and neck OARs and then arbitrated by a second radiographer with similar experience. Further arbitration was then performed by a radiation oncologist with at least five years post-certification experience in head and neck radiotherapy. The same process was repeated with two additional radiographers working independently but after peer arbitration these segmentations were not reviewed by an oncologist; rather they became the human reference to which the model was compared. This is shown schematically in [Fig. 6](#). Prior to participation all radiographers and oncologists were required to study the Brouwer Atlas for head and neck OAR segmentation [49] and demonstrate competence in adhering to these guidelines.

4.4 Model architecture

We used a residual 3D U-Net architecture with 8 levels (see [Fig. 7](#)). Our network takes in a CT volume (single channel) and outputs a segmentation mask with 21 channels, where each channel contains the binary segmentation mask for a specific OAR. Due to the unpadded convolutions in the z-direction, the output volume has 20 slices less than the input volume. The network consists of 7 residual convolutional blocks in the downward path, a residual fully connected block at the bottom, and 7 residual convolutional

Table 3 | Taxonomy of segmentation regions.

OAR	Total number of labelled slices included	Anatomical Landmarks and Definition
Brain	5847	Sits inside the cranium and includes all brain vessels excluding the brainstem and optic chiasm.
Brainstem	8559	The posterior aspect of the brain including the midbrain, pons and medulla oblongata. Extending inferior from the lateral ventricles to the tip of the dens at C2. It is structurally continuous with the spinal cord.
Cochlea-Lt	1786	Embedded in the temporal bone and lateral to the internal auditory meatus.
Cochlea-Rt	1819	
Lacrimal-Lt	13038	Concave shaped gland located at the superolateral aspect of the orbit.
Lacrimal-Rt	12976	
Lens-Lt	5341	An oval structure that sits within the anterior segment of the orbit. Can be variable in position but never sitting posterior beyond the level of the outer canthus.
Lens-Rt	5407	
Lung-Lt	4690	Encompassed by the thoracic cavity adjacent to the lateral aspect of the mediastinum, extending from the 1st rib to the diaphragm excluding the carina.
Lung-Rt	4990	
Mandible	9722	The entire mandible bone including the temporomandibular joint, ramus and body, excluding the teeth. The mandible joins to the inferior aspect of the temporal bone and forms the entire lower jaw.
Optic-Nerve-Lt	2111	A 2-5mm thick nerve that runs from the posterior aspect of the eye, through the optic canal and ends at the lateral aspect of the optic chiasm.
Optic-Nerve-Rt	1931	
Orbit-Lt	4117	Spherical organ sitting within the orbital cavity. Includes the vitreous humor, retina, cornea and lens with the optic nerve attached posteriorly.
Orbit-Rt	3900	
Parotid-Lt	5182	Multi lobed salivary gland wrapped around the mandibular ramus. Extends medially to styloid process and parapharyngeal space. Laterally extending to subcutaneous fat. Posteriorly extending to sternocleidomastoid muscle. Anterior extending to posterior border of mandible bone and masseter muscle. In cases where retromandibular vein is encapsulated by parotid this is included in the segmentation.
Parotid-Rt	6646	
Spinal-Canal	23100	Hollow cavity that runs through the foramen of the vertebrae, extending from the base of skull to the end of the sacrum.
Spinal-Cord	22460	Sits inside the Spinal Canal and extends from the level of the foramen magnum to the bottom of L2.
Submandibular-Lt	4313	Sits within the submandibular portion of the anterior triangle of the neck, making up the floor of the mouth and extending both superior and inferior to the posterior aspect of the mandible and is limited laterally by the mandible and medially by the hypoglossal muscle.
Submandibular-Rt	4473	

blocks in the upward path. A $1 \times 1 \times 1$ convolution layer with sigmoidal activation produces the final output in the original resolution of the input image.

We trained our network with a regularised top-k-percent pixel-wise binary cross-entropy loss [43]: for each output channel, we selected the top 5% most difficult pixels (those with the highest binary cross-entropy) and only added their contribution to the total loss. This speeds up training and helps the network to tackle the large class imbalance and to focus on difficult examples.

We regularised the model using standard L2 weight regularisation with scale 10^{-6} and extensive data augmentation: we used random in-plane (i.e. in x- and y- directions only) translation, rotation, scaling,

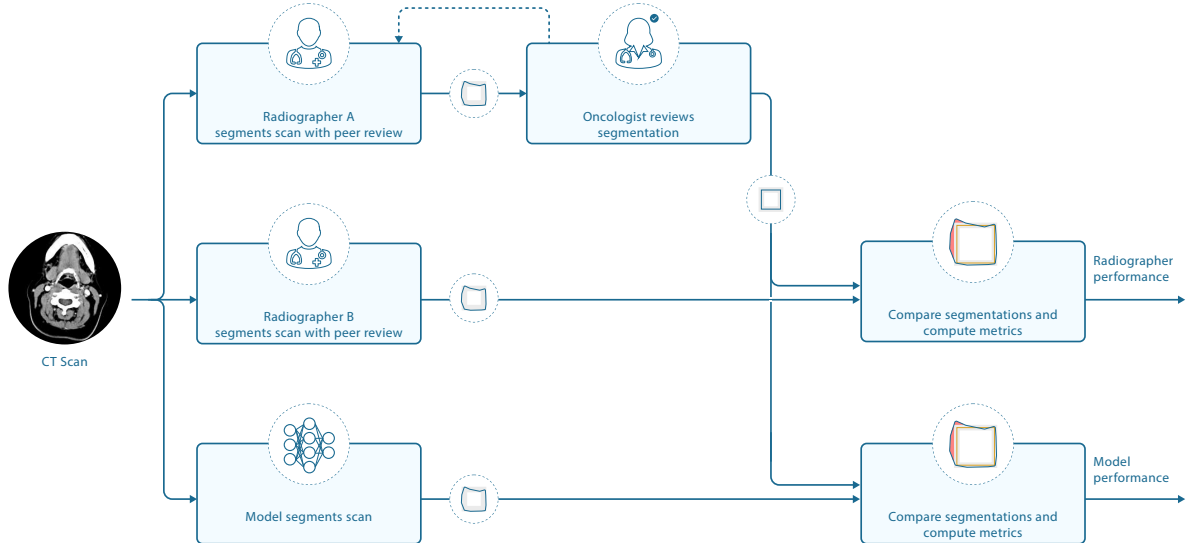


Figure 6 | Process for segmentation of ground truth and radiographer OAR volumes. The flowchart illustrates how the ground truth segmentations were created and compared with independent radiographer segmentations and the model. For the ground truth each CT scan in the TCIA test set was segmented first by a radiographer and peer reviewed by a second radiographer. This then went through one or more iterations of review and editing with a specialist oncologist before creating a ground truth used to compare with the segmentations produced by both the model and additional radiographers.

shearing, mirroring, elastic deformations, and pixel-wise noise. We used uniform translations between -32 and 32 pixels; uniform rotations between -9 and 9 degrees; uniform scaling factors between 0.8 and 1.2; and uniform shear factors between -0.1 and 0.1. We mirrored images (and adjusted corresponding left and right labels) with a probability of 0.5. We performed elastic deformations by placing random displacement vectors (standard deviation: 5mm, in-plane displacements only) on a control point grid with 100mm x 100mm x 100mm spacing and by deriving the dense deformation field using cubic b-spline interpolation. In the implementation all spatial transformations are first combined to a dense deformation field, which is then applied to the image using bilinear interpolation and extrapolation with zero padding. We added zero mean Gaussian intensity noise independently to each pixel with a standard deviation of 20 Hounsfield Units.

We trained the model with the Adam optimiser [51] for 120,000 steps and a batch size of 32 (32 GPUs) using synchronous SGD. We used an initial learning rate of 10^{-4} and scaled the learning rate by 1/2, 1/8, 1/64, and 1/256 at timesteps 24,000, 60,000, 108,000, and 114,000, respectively.

We used the validation set to select the model which performed at over 95% for the most OARs according to our chosen surface DSC performance metric, breaking ties by preferring better performance on more clinically impactful OARs and the absolute performance obtained.

4.5 Performance metrics

All performance metrics are reported for each organ independently (e.g., separately for just the left Parotid), so we only need to deal with binary masks (e.g. a left parotid voxel and a non left-parotid voxel). Masks are defined as a subset of \mathbb{R}^3 , i.e. $\mathcal{M} \subset \mathbb{R}^3$ (see Fig. 8).

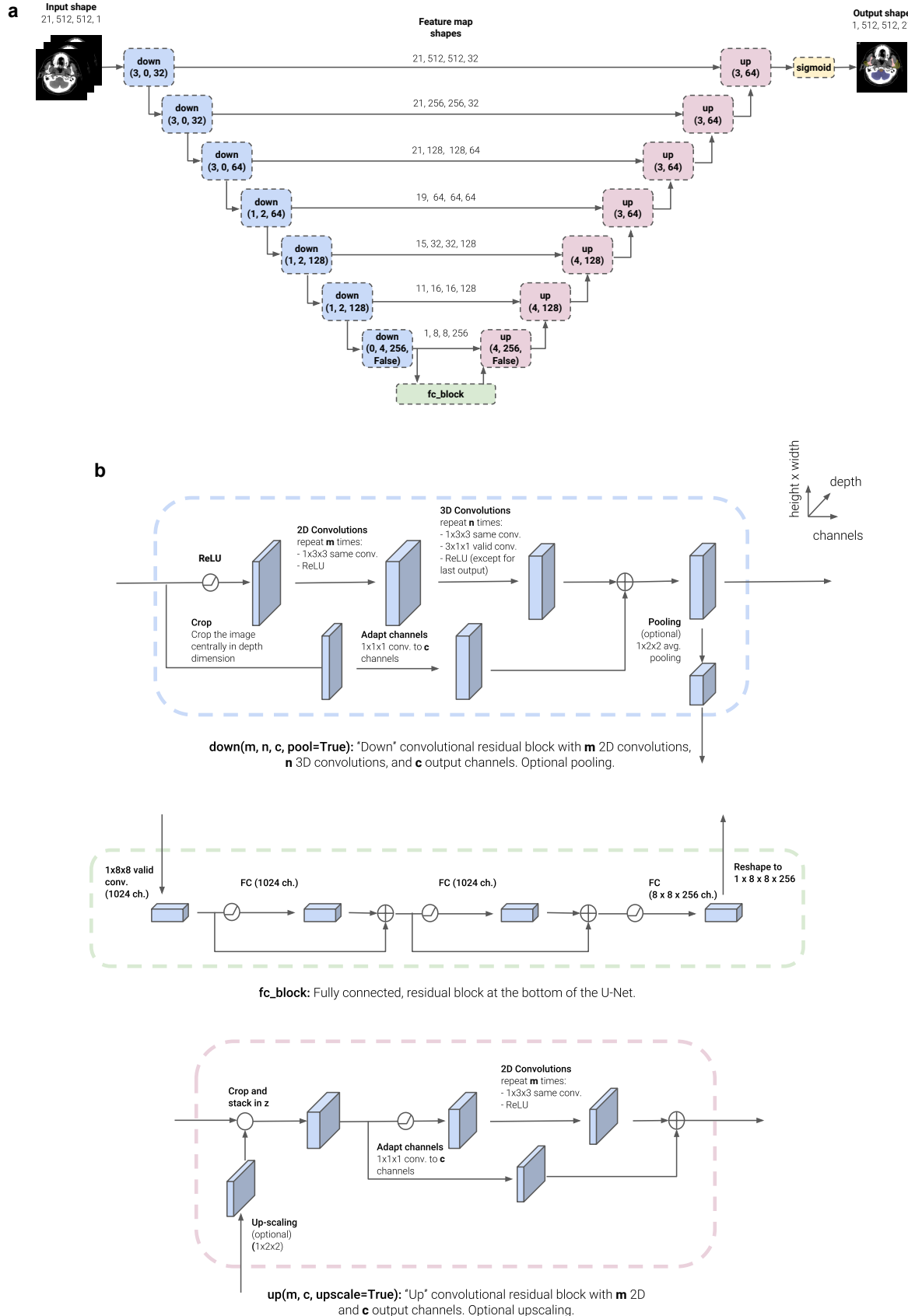


Figure 7 | 3D U-Net model architecture. (a) At training time, the model receives 21 contiguous CT slices, which are processed through a series of “down” blocks, a fully connected block, and a series of “up” blocks to create a segmentation prediction. (b) A detailed view of the convolutional residual up and down blocks, and the residual fully connected block.

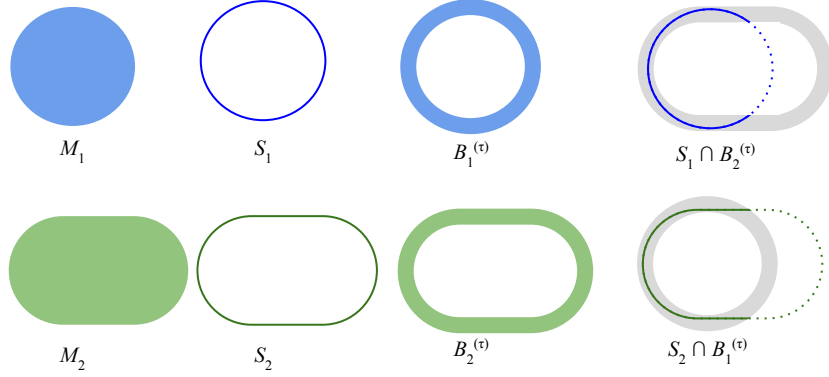


Figure 8 | Illustrations of masks, surfaces, border regions, and the “overlapping” surface at tolerance τ

The volume of a mask is denoted as $|\cdot|$, with

$$|\mathcal{M}| = \int_{\mathcal{M}} d\mathbf{x}.$$

With this notation the standard (volumetric) DSC for two given masks \mathcal{M}_1 and \mathcal{M}_2 can be written as

$$C_{\text{DSC}} = \frac{2 |\mathcal{M}_1 \cap \mathcal{M}_2|}{|\mathcal{M}_1| + |\mathcal{M}_2|}.$$

In the case of sparse ground truth segmentations (i.e. only a few slices of the CT scan are labelled), we estimate the volumetric DSC by aggregating data from labelled voxels across multiple scans as

$$C_{\text{DSC, est}} = \frac{2 \sum_p |\mathcal{M}_{1,p} \cap \mathcal{M}_{2,p} \cap \mathcal{L}_p|}{\sum_p |\mathcal{M}_{1,p} \cap \mathcal{L}_p| + |\mathcal{M}_{2,p} \cap \mathcal{L}_p|},$$

where the mask $\mathcal{M}_{1,p}$ and the labelled region \mathcal{L}_p represent the sparse ground truth segmentation for a patient p and the mask $\mathcal{M}_{2,p}$ is the full volume predicted segmentation for patient p .

Due to the shortcomings of the volumetric DSC metric for the presented radiotherapy use case, we introduce the “surface DSC” metric, which assesses the overlap of two surfaces (at a specified tolerance) instead of the overlap of two volumes (see Results section). A surface is the border of a mask, $\mathcal{S} = \partial \mathcal{M}$, the area of a surface is denoted as

$$|\mathcal{S}| = \int_{\mathcal{S}} d\boldsymbol{\sigma}$$

where $\boldsymbol{\sigma} \in \mathcal{S}$ is a point on the surface, using an arbitrary parameterisation. The mapping from this parameterisation to a point in \mathbb{R}^3 is denoted as $\xi : \mathcal{S} \rightarrow \mathbb{R}^3$, i.e. $\mathbf{x} = \xi(\boldsymbol{\sigma})$. With this we can define the border region $\mathcal{B}_i^{(\tau)} \subset \mathbb{R}^3$, for the surface \mathcal{S}_i , at a given tolerance τ as

$$\mathcal{B}_i^{(\tau)} = \left\{ \mathbf{x} \in \mathbb{R}^3 \mid \exists \boldsymbol{\sigma} \in \mathcal{S}_i, \|\mathbf{x} - \xi(\boldsymbol{\sigma})\| \leq \tau \right\},$$

(see Fig. 8 for an example). Using these definitions we can write the “surface DSC at tolerance τ ” as

$$R_{i,j}^{(\tau)} = \frac{|\mathcal{S}_i \cap \mathcal{B}_j^{(\tau)}| + |\mathcal{S}_j \cap \mathcal{B}_i^{(\tau)}|}{|\mathcal{S}_i| + |\mathcal{S}_j|},$$

using an informal notation for the intersection of the surface with the boundary, i.e.:

$$\left| \mathcal{S}_i \cap \mathcal{B}_j^{(\tau)} \right| := \int_{\mathcal{S}_i} \mathbb{1}_{\mathcal{B}_j^{(\tau)}} (\xi(\sigma)) d\sigma$$

4.6 Implementation

The computation of surface integrals on sampled images is not straightforward, especially for medical images, where the voxel spacing is usually not equal in all three dimensions. The common approximation of the integral by counting surface voxels can lead to substantial systematic errors.

Another common challenge is the representation of the surface with voxels. As the surface of a binary mask is located between voxels, a definition of “surface voxels” in the raster-space of the image introduces a bias: using foreground voxels to represent the surface leads to an underestimation of the surface, while the use of background voxels leads to an overestimation.

Our proposed implementation uses a surface representation that provides less biased estimates but still allows us to compute the performance metrics with linear complexity ($\mathcal{O}(N)$, with N : number of voxels). We place the surface points between the voxels on a raster that is shifted by half of the raster spacing on each axis (see Fig. 9 for a 2D illustration). For 3D images, each point in this raster has 8 neighbouring

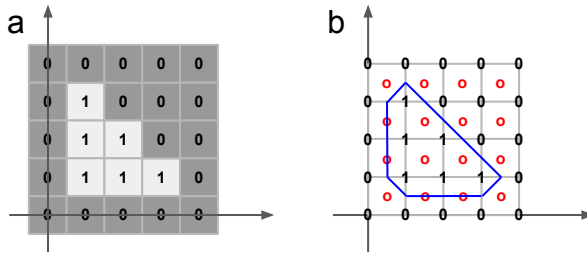


Figure 9 | 2D illustration of the implementation of the surface DSC. (a) A binary mask displayed as image. The origin of the image raster is (0,0). (b) The surface points (red circles) are located in a raster that is shifted half of the raster spacing on each axis. Each surface point has 4 neighbours in 2D (8 neighbours in 3D). The local contour (blue line) assigned to each surface point (red circle) depends on the neighbour constellation.

voxels. As we analyse binary masks, there are only $2^8 = 256$ possible neighbour constellations. For each of these constellations we compute the resulting triangles using the marching cube triangulation [52] and store the surface area of the triangles (in mm^2) in a look-up table. With this look-up table we then create a surface image (on the above mentioned raster) that contains zeros at positions that have 8 identical neighbours or the local surface area at all positions that have both foreground and background neighbours. These surface images are created for the masks \mathcal{M}_1 and \mathcal{M}_2 . Additionally we create a distance map from each of these surface images using the distance transform algorithm [53]. Iterating over the non-zero elements in the first surface image and looking up the distance from the other surface in the corresponding distance map allows to create a list of tuples (surface element area, distance from other surface). From this list we can easily compute the surface area by summing up the area of the surface elements that are within the tolerance. To account for the quantised distances – there is only a discrete set $\mathcal{D} = \left\{ \sqrt{(n_1 d_1)^2 + (n_2 d_2)^2 + (n_3 d_3)^2} \mid n_1, n_2, n_3 \in \mathbb{N} \right\}$ of distances between voxels in a 3D raster with spacing (d_1, d_2, d_3) – we also round the tolerance to the nearest neighbour in the set \mathcal{D} for each image before computing the surface DSC. For more details, please have a look at our open source implementation of the surface DSC, available from <https://github.com/deepmind/surface-distance>.

5 Code availability

The codebase for the deep learning framework makes use of proprietary components and we are unable to publicly release this code. However, all experiments and implementation details are described in sufficient detail in the methods section to allow independent replication with non-proprietary libraries. The surface DSC performance metric code is available at <https://github.com/deepmind/surface-distance>.

6 Data availability

The clinical data used for training and validation sets were collected at University College London Hospitals NHS Foundation Trust and transferred to the DeepMind data centre in the UK in de-identified format. Data were used with both local and national permissions. They are not publicly available and restrictions apply to their use. The data, or a subset, may be available from UCLH NHS Foundation Trust subject to local and national ethical approvals. The released test/validation set data was collected from two datasets hosted on The Cancer Imaging Archive (TCIA). The subset used, along with the ground truth segmentations added is available at <https://github.com/deepmind/tcia-ct-scan-dataset>.

7 Acknowledgement

We thank the patients treated at UCLH whose scans were used in the work, A. Zisserman, D. King, D. Barrett, V. Cornelius, C. Beltram, J. Cornebise, J. Ashburner, J. Good and N. Haji for discussions, M. Kosmin for his review of the published literature, A. Warry, U. Johnson, V. Rompokos and the rest of the UCLH Radiotherapy Physics team for work on the data collection, R. West for work on the visuals, C. Game, D. Mitchell and M. Johnson for infrastructure and systems administration, A. Paine at Softwire for engineering support at UCLH, A. Kitchener and the UCLH Information Governance team for support, J. Besley and M. Bawn for legal assistance, K. Ayoub and R. Ahmed for initiating and supporting the collaboration, the DeepMind Radiographer Consortium made up of B. Hatchard, Y. McQuinlan, K. Hampton, S. Ireland, K. Fuller, H. Frank, C. Tully, A. Jones and L. Turner, and the rest of the DeepMind team for their support, ideas and encouragement.

G.R., H.M. and R.S. were supported by University College London and the National Institute for Health Research (NIHR) University College London Hospitals Biomedical Research Centre. The views expressed are those of the author(s) and not necessarily those of the NHS, the NIHR or the Department of Health.

8 Author contributions

M.S., T.B., O.R., J.L., R.M., H.M., S.A.M., D.D'S., C.C., & K.S. initiated the project

S.B., R.M., D.C., C.B., D.D'S., C.C. & J.L., created the dataset

S.B., S.N., J.D.F., C.H., H.A. & O.R. contributed to software engineering

S.N., J.D.F., B.R.P. & O.R. designed the model architectures

D.R.C. manually segmented the images

R.M., D.C., C.B., D.D'S., S.A.M., H.M., G.R., R.S., C.H., A.K. & J.L. contributed clinical expertise

C.M., J.L., T.B., S.A.M., K.S. & O.R. managed the project

J.L., S.N., S.B., J.D.F., H.M., G.R., R.S. & O.R. wrote the paper

9 Competing financial interests

R.S, G.R., H.M. and D.R.C are paid contractors of DeepMind. The authors have no other competing interests to disclose.

References

- [1] A. Jemal, F. Bray, M. M. Center, J. Ferlay, E. Ward, and D. Forman, “Global cancer statistics,” *CA Cancer J. Clin.*, vol. 61, no. 2, pp. 69–90, Mar. 2011. Available: <http://dx.doi.org/10.3322/caac.20107>
- [2] Cancer Research UK, “Head and neck cancers incidence statistics,” <https://www.cancerresearchuk.org/health-professional/cancer-statistics/statistics-by-cancer-type/head-and-neck-cancers/incidence#heading-Two>, Feb. 2018, accessed: 2018-2-8.
- [3] National Cancer Intelligence Network, “NCIN data briefing: Potentially HPV-related head and neck cancers,” http://www.ncin.org.uk/publications/data_briefings/potentially_hpv_related_head_and_neck_cancers, May 2012.
- [4] Oxford Cancer Intelligence Unit, “Profile of head and neck cancers in england: Incidence, mortality and survival,” National Cancer Intelligence Network, Tech. Rep., 2010. Available: <http://www.ncin.org.uk/view?rid=69>
- [5] D. M. Parkin, L. Boyd, and L. C. Walker, “16. the fraction of cancer attributable to lifestyle and environmental factors in the UK in 2010,” *Br. J. Cancer*, vol. 105, no. S2, pp. S77–81, 2011. Available: <http://dx.doi.org/10.1038/bjc.2011.489>
- [6] K. Jensen, K. Lambertsen, and C. Grau, “Late swallowing dysfunction and dysphagia after radiotherapy for pharynx cancer: frequency, intensity and correlation with dose and volume parameters,” *Radiother. Oncol.*, vol. 85, no. 1, pp. 74–82, Oct. 2007. Available: <http://dx.doi.org/10.1016/j.radonc.2007.06.004>
- [7] P. Dirix, S. Abbeel, B. Vanstraelen, R. Hermans, and S. Nuyts, “Dysphagia after chemoradiotherapy for head-and-neck squamous cell carcinoma: Dose–effect relationships for the swallowing structures,” *Int J Radiat Oncol Biol Phys*, vol. 75, no. 2, pp. 385–392, Oct. 2009. Available: <https://doi.org/10.1016/j.ijrobp.2008.11.041>
- [8] J. J. Caudell, P. E. Schaner, R. A. Desmond, R. F. Meredith, S. A. Spencer, and J. A. Bonner, “Dosimetric factors associated with long-term dysphagia after definitive radiotherapy for squamous cell carcinoma of the head and neck,” *Int. J. Radiat. Oncol. Biol. Phys.*, vol. 76, no. 2, pp. 403–409, Feb. 2010. Available: <http://dx.doi.org/10.1016/j.ijrobp.2009.02.017>
- [9] C. M. Nutting, J. P. Morden, K. J. Harrington, T. G. Urbano, S. A. Bhide, C. Clark, E. A. Miles, A. B. Miah, K. Newbold, M. Tanay, F. Adab, S. J. Jefferies, C. Scrase, B. K. Yap, R. P. A’Hern, M. A. Sydenham, M. Emson, E. Hall, and PARSPORT trial management group, “Parotid-sparing intensity modulated versus conventional radiotherapy in head and neck cancer (PARSPORT): a phase 3 multicentre randomised controlled trial,” *Lancet Oncol.*, vol. 12, no. 2, pp. 127–136, Feb. 2011. Available: [http://dx.doi.org/10.1016/S1470-2045\(10\)70290-4](http://dx.doi.org/10.1016/S1470-2045(10)70290-4)

- [10] B. E. Nelms, W. A. Tomé, G. Robinson, and J. Wheeler, “Variations in the contouring of organs at risk: test case from a patient with oropharyngeal cancer,” *Int. J. Radiat. Oncol. Biol. Phys.*, vol. 82, no. 1, pp. 368–378, Jan. 2012. Available: <http://dx.doi.org/10.1016/j.ijrobp.2010.10.019>
- [11] P. W. J. Voet, M. L. P. Dirkx, D. N. Teguh, M. S. Hoogeman, P. C. Levendag, and B. J. M. Heijmen, “Does atlas-based autosegmentation of neck levels require subsequent manual contour editing to avoid risk of severe target underdosage? a dosimetric analysis,” *Radiother. Oncol.*, vol. 98, no. 3, pp. 373–377, Mar. 2011. Available: <http://dx.doi.org/10.1016/j.radonc.2010.11.017>
- [12] P. M. Harari, S. Song, and W. A. Tomé, “Emphasizing conformal avoidance versus target definition for IMRT planning in head-and-neck cancer,” *Int. J. Radiat. Oncol. Biol. Phys.*, vol. 77, no. 3, pp. 950–958, Jul. 2010. Available: <http://dx.doi.org/10.1016/j.ijrobp.2009.09.062>
- [13] Z. Chen, W. King, R. Pearcey, M. Kerba, and W. J. Mackillop, “The relationship between waiting time for radiotherapy and clinical outcomes: a systematic review of the literature,” *Radiother. Oncol.*, vol. 87, no. 1, pp. 3–16, Apr. 2008. Available: <http://dx.doi.org/10.1016/j.radonc.2007.11.016>
- [14] J. S. Mikeljevic, R. Haward, C. Johnston, A. Crellin, D. Dodwell, A. Jones, P. Pisani, and D. Forman, “Trends in postoperative radiotherapy delay and the effect on survival in breast cancer patients treated with conservation surgery,” *Br. J. Cancer*, vol. 90, no. 7, pp. 1343–1348, Apr. 2004. Available: <http://dx.doi.org/10.1038/sj.bjc.6601693>
- [15] C. E. Round, M. V. Williams, T. Mee, N. F. Kirkby, T. Cooper, P. Hoskin, and R. Jena, “Radiotherapy demand and activity in england 2006-2020,” *Clin. Oncol.*, vol. 25, no. 9, pp. 522–530, Sep. 2013. Available: <http://dx.doi.org/10.1016/j.clon.2013.05.005>
- [16] Z. E. Rosenblatt E, “Radiotherapy in cancer care: Facing the global challenge,” International Atomic Energy Agency, Tech. Rep., 2017. Available: https://www-pub.iaea.org/MTCD/Publications/PDF/P1638_web.pdf
- [17] C. Veiga, J. McClelland, S. Moinuddin, A. Lourenço, K. Ricketts, A. J, M. Modat, O. S, D. D’Souza, and G. Royle, “Toward adaptive radiotherapy for head and neck patients: Feasibility study on using ct-to-cbct deformable registration for ‘dose of the day’ calculations,” *Med. Phys.*, vol. 41, no. 3, p. 031703 (12pp.), 2014. Available: <https://doi.org/10.1118/1.4864240>
- [18] J.-F. Daisne and A. Blumhofer, “Atlas-based automatic segmentation of head and neck organs at risk and nodal target volumes: a clinical validation,” *Radiat. Oncol.*, vol. 8, p. 154, Jun. 2013. Available: <http://dx.doi.org/10.1186/1748-717X-8-154>
- [19] V. Fortunati, R. F. Verhaart, F. van der Lijn, W. J. Niessen, J. F. Veenland, M. M. Paulides, and T. van Walsum, “Tissue segmentation of head and neck CT images for treatment planning: a multiatlas approach combined with intensity modeling,” *Med. Phys.*, vol. 40, no. 7, p. 071905, Jul. 2013. Available: <http://dx.doi.org/10.1118/1.4810971>
- [20] H. Duc, K. Albert, G. Eminowicz, R. Mendes, S.-L. Wong, J. McClelland, M. Modat, M. J. Cardoso, A. F. Mendelson, C. Veiga, and Others, “Validation of clinical acceptability of an atlas-based segmentation algorithm for the delineation of organs at risk in head and neck cancer,” *Med. Phys.*, vol. 42, no. 9, pp. 5027–5034, 2015. Available: <https://doi.org/10.1118/1.4927567>
- [21] M. S. Hoogeman, X. Han, D. Teguh, P. Voet, P. Nowak, T. Wolf, L. Hibbard, B. Heijmen, and P. Levendag, “Atlas-based auto-segmentation of CT images in head and neck cancer: What is the best approach?” *Int. J. Radiat. Oncol. Biol. Phys.*, vol. 72, no. 1, p. S591, Sep. 2008. Available: <https://doi.org/10.1016/j.ijrobp.2008.06.196>

- [22] P. C. Levendag, M. Hoogeman, D. Teguh, T. Wolf, L. Hibbard, O. Wijers, B. Heijmen, P. Nowak, E. Vasquez-Osorio, and X. Han, “Atlas based auto-segmentation of CT images: clinical evaluation of using auto-contouring in high-dose, high-precision radiotherapy of cancer in the head and neck,” *Int. J. Radiat. Oncol. Biol. Phys.*, vol. 72, no. 1, p. S401, Sep. 2008. Available: <https://doi.org/10.1016/j.ijrobp.2008.06.1285>
- [23] A. A. Qazi, V. Pekar, J. Kim, J. Xie, S. L. Breen, and D. A. Jaffray, “Auto-segmentation of normal and target structures in head and neck CT images: A feature-driven model-based approach,” *Med. Phys.*, vol. 38, no. 11, pp. 6160–6170, 2011. Available: <https://doi.org/10.1118/1.3654160>
- [24] R. Sims, A. Isambert, V. Grégoire, F. Bidault, L. Fresco, J. Sage, J. Mills, J. Bourhis, D. Lefkopoulos, O. Commowick, M. Benkebil, and G. Malandain, “A pre-clinical assessment of an atlas-based automatic segmentation tool for the head and neck,” *Radiother. Oncol.*, vol. 93, no. 3, pp. 474–478, Dec. 2009. Available: <http://dx.doi.org/10.1016/j.radonc.2009.08.013>
- [25] D. N. Teguh, P. C. Levendag, P. W. J. Voet, A. Al-Mamgani, X. Han, T. K. Wolf, L. S. Hibbard, P. Nowak, H. Akhiat, M. L. P. Dirkx, B. J. M. Heijmen, and M. S. Hoogeman, “Clinical validation of atlas-based auto-segmentation of multiple target volumes and normal tissue (swallowing/mastication) structures in the head and neck,” *Int. J. Radiat. Oncol. Biol. Phys.*, vol. 81, no. 4, pp. 950–957, Nov. 2011. Available: <http://dx.doi.org/10.1016/j.ijrobp.2010.07.009>
- [26] D. Thomson, C. Boylan, T. Liptrot, A. Aitkenhead, L. Lee, B. Yap, A. Sykes, C. Rowbottom, and N. Slevin, “Evaluation of an automatic segmentation algorithm for definition of head and neck organs at risk,” *Radiat. Oncol.*, vol. 9, p. 173, Aug. 2014. Available: <http://dx.doi.org/10.1186/1748-717X-9-173>
- [27] G. V. Walker, M. Awan, R. Tao, E. J. Koay, N. S. Boehling, J. D. Grant, D. F. Sittig, G. B. Gunn, A. S. Garden, J. Phan, W. H. Morrison, D. I. Rosenthal, A. S. R. Mohamed, and C. D. Fuller, “Prospective randomized double-blind study of atlas-based organ-at-risk autosegmentation-assisted radiation planning in head and neck cancer,” *Radiother. Oncol.*, vol. 112, no. 3, pp. 321–325, Sep. 2014. Available: <http://dx.doi.org/10.1016/j.radonc.2014.08.028>
- [28] O. Ronneberger, P. Fischer, and T. Brox, “U-Net: convolutional networks for biomedical image segmentation,” in *Med Image Comput Comput Assist Interv.* Springer International Publishing, 2015, pp. 234–241. Available: http://dx.doi.org/10.1007/978-3-319-24574-4_28
- [29] J. De Fauw, J. R. Ledsam, B. Romera-Paredes, S. Nikolov, N. Tomasev, S. Blackwell, H. Askham, X. Glorot, B. O’Donoghue, D. Visentin, G. van den Driessche, B. Lakshminarayanan, C. Meyer, F. Mackinder, S. Bouton, K. Ayoub, R. Chopra, D. King, A. Karthikesalingam, C. O. Hughes, R. Raine, J. Hughes, D. A. Sim, C. Egan, A. Tufail, H. Montgomery, D. Hassabis, G. Rees, T. Back, P. T. Khaw, M. Suleyman, J. Cornebise, P. A. Keane, and O. Ronneberger, “Clinically applicable deep learning for diagnosis and referral in retinal disease,” *Nat. Med.*, vol. 24, pp. 1342–1350, Aug. 2018. Available: <http://dx.doi.org/10.1038/s41591-018-0107-6>
- [30] K. Fritscher, P. Raudaschl, P. Zaffino, M. F. Spadea, G. C. Sharp, and R. Schubert, “Deep neural networks for fast segmentation of 3D medical images,” in *Med Image Comput Comput Assist Interv.* Springer International Publishing, 2016, pp. 158–165. Available: http://dx.doi.org/10.1007/978-3-319-46723-8_19
- [31] B. Ibragimov and L. Xing, “Segmentation of organs-at-risks in head and neck CT images using convolutional neural networks,” *Med. Phys.*, vol. 44, no. 2, pp. 547–557, 2017. Available: <https://doi.org/10.1118/1.3654160>

- [32] D. Močnik, B. Ibragimov, L. Xing, P. Strojan, B. Likar, F. Pernuš, and T. Vrtovec, “Segmentation of parotid glands from registered CT and MR images,” *Phys. Med.*, vol. 52, pp. 33–41, Aug. 2018. Available: <https://doi.org/10.1016/j.ejmp.2018.06.012>
- [33] X. Ren, L. Xiang, D. Nie, Y. Shao, H. Zhang, D. Shen, and Q. Wang, “Interleaved 3D-CNNs for joint segmentation of small-volume structures in head and neck CT images,” *Med. Phys.*, vol. 45, no. 5, pp. 2063–2075, May 2018. Available: <http://dx.doi.org/10.1002/mp.12837>
- [34] A. Hänsch, M. Schwier, T. Gass, T. Morgas, B. Haas, J. Klein, and H. K. Hahn, “Comparison of different deep learning approaches for parotid gland segmentation from CT images,” in *Med Imaging Comp-Aided Diag*, vol. 10575. International Society for Optics and Photonics, Feb. 2018, p. 1057519. Available: <https://doi.org/10.1117/12.2292962>
- [35] W. Zhu, Y. Huang, H. Tang, Z. Qian, N. Du, W. Fan, and X. Xie, “AnatomyNet: Deep 3D squeeze-and-excitation U-Nets for fast and fully automated whole-volume anatomical segmentation,” Aug. 2018, arXiv preprint [arXiv:1808.05238](https://arxiv.org/abs/1808.05238).
- [36] N. Tong, S. Gou, S. Yang, D. Ruan, and K. Sheng, “Fully automatic multi-organ segmentation for head and neck cancer radiotherapy using shape representation model constrained fully convolutional neural networks,” *Medical Physics*, vol. 0, no. ja, 2018. Available: <https://doi.org/10.1002/mp.13147>
- [37] W. R. Bosch, W. L. Straube, J. W. Matthews, and J. A. Purdy, “Head-neck cetuximab - the cancer imaging archive,” 2015. Available: <https://wiki.cancerimagingarchive.net/display/Public/Head-Neck+Cetuximab>
- [38] K. Clark, B. Vendt, K. Smith, J. Freymann, J. Kirby, P. Koppel, S. Moore, S. Phillips, D. Maffitt, M. Pringle, L. Tarbox, and F. Prior, “The cancer imaging archive (TCIA): maintaining and operating a public information repository,” *J Digit Imaging*, vol. 26, no. 6, pp. 1045–1057, Dec. 2013. Available: <http://dx.doi.org/10.1007/s10278-013-9622-7>
- [39] M. L. Zuley, R. Jarosz, S. Kirk, L. Y., R. Colen, K. Garcia, and N. D. Arede, “Radiology data from the cancer genome atlas head-neck squamous cell carcinoma [TCGA-HNSC] collection,” 2016. Available: <http://dx.doi.org/10.7937/K9/TCIA.2016.LXKQ47MS>
- [40] C. Chu, D. F. J, T. N, B. Romera-Paredes, C. Hughes, J. Ledsam, T. Back, H. Montgomery, G. Rees, R. Raine, K. Sullivan, S. Moinuddin, D. D’Souza, O. Ronneberger, R. Mendes, and J. Cornebise, “Applying machine learning to automated segmentation of head and neck tumour volumes and organs at risk on radiotherapy planning ct and mri scans,” *F1000 Research*, vol. 5, no. 2104, 2016. Available: <http://dx.doi.org/10.12688/f1000research.9525.1>
- [41] Ö. Çiçek, A. Abdulkadir, S. S. Lienkamp, T. Brox, and O. Ronneberger, “3D U-Net: learning dense volumetric segmentation from sparse annotation,” in *Med Image Comput Comput Assist Interv*, 2016, pp. 424–432. Available: https://doi.org/10.1007/978-3-319-46723-8_49
- [42] K. He, X. Zhang, S. Ren, and J. Sun, “Deep residual learning for image recognition,” Dec. 2015, arXiv preprint [arXiv:1512.03385](https://arxiv.org/abs/1512.03385).
- [43] Z. Wu, C. Shen, and A. v. D. Hengel, “Bridging category-level and instance-level semantic image segmentation,” May 2016, arXiv preprint [arXiv:1605.06885v1](https://arxiv.org/abs/1605.06885v1).
- [44] L. R. Dice, “Measures of the amount of ecologic association between species,” *Ecology*, vol. 26, no. 3, pp. 297–302, Jul. 1945. Available: <http://doi.wiley.com/10.2307/1932409>

- [45] P. F. Raudaschl, P. Zaffino, G. C. Sharp, M. F. Spadea, A. Chen, B. M. Dawant, T. Albrecht, T. Gass, C. Langguth, M. Lüthi, and Others, “Evaluation of segmentation methods on head and neck CT: Auto-segmentation challenge 2015,” *Med. Phys.*, vol. 44, no. 5, pp. 2020–2036, 2017. Available: <https://doi.org/10.1002/mp.12197>
- [46] C. M. Tam, X. Yang, S. Tian, X. Jiang, J. J. Beitler, and S. Li, “Automated delineation of organs-at-risk in head and neck CT images using multi-output support vector regression,” in *Medical Imaging 2018: Biomedical Applications in Molecular, Structural, and Functional Imaging*, vol. 10578. International Society for Optics and Photonics, Mar. 2018, p. 1057824. Available: <https://doi.org/10.1117/12.2292556>
- [47] Z. Wang, L. Wei, L. Wang, Y. Gao, W. Chen, and D. Shen, “Hierarchical vertex regression-based segmentation of head and neck CT images for radiotherapy planning,” *IEEE Trans. Image Process.*, vol. 27, no. 2, pp. 923–937, Feb. 2018. Available: <http://dx.doi.org/10.1109/TIP.2017.2768621>
- [48] E. J. Wuthrick, Q. Zhang, M. Machtay, D. I. Rosenthal, P. F. Nguyen-Tan, A. Fortin, C. L. Silverman, A. Raben, H. E. Kim, E. M. Horwitz, N. E. Read, J. Harris, Q. Wu, Q.-T. Le, and M. L. Gillison, “Institutional clinical trial accrual volume and survival of patients with head and neck cancer,” *Journal of Clinical Oncology*, vol. 33, no. 2, pp. 156–164, 2015, pMID: 25488965. Available: <https://doi.org/10.1200/JCO.2014.56.5218>
- [49] C. L. Brouwer, R. J. H. M. Steenbakkers, J. Bourhis, W. Budach, C. Grau, V. Grégoire, M. van Herk, A. Lee, P. Maingon, C. Nutting, B. O’Sullivan, S. V. Porceddu, D. I. Rosenthal, N. M. Sijtsema, and J. A. Langendijk, “CT-based delineation of organs at risk in the head and neck region: DAHANCA, EORTC, GORTEC, HKNPCSG, NCIC CTG, NCRI, NRG oncology and TROG consensus guidelines,” *Radiother. Oncol.*, vol. 117, no. 1, pp. 83–90, Oct. 2015. Available: <http://dx.doi.org/10.1016/j.radonc.2015.07.041>
- [50] G. Sharp, K. D. Fritscher, V. Pekar, M. Peroni, N. Shusharina, H. Veeraraghavan, and J. Yang, “Vision 20/20: perspectives on automated image segmentation for radiotherapy,” *Med. Phys.*, vol. 41, no. 5, p. 050902, May 2014. Available: <http://dx.doi.org/10.1118/1.4871620>
- [51] D. P. Kingma and J. Ba, “Adam: a method for stochastic optimization,” Dec. 2014, arXiv preprint [arXiv:1412.6980](https://arxiv.org/abs/1412.6980).
- [52] W. E. Lorensen and H. E. Cline, “Marching cubes: A high resolution 3D surface construction algorithm,” *Comp. Graph.*, vol. 21, no. 4, pp. 163–169, 1987. Available: [http://doi.acm.org/10.1145/37401.37422](https://doi.acm.org/10.1145/37401.37422)
- [53] P. F. Felzenszwalb and D. P. Huttenlocher, “Distance transforms of sampled functions,” *Theory Comput.*, vol. 8, no. 19, pp. 415–428, 2012. Available: <http://dx.doi.org/10.4086/toc.2012.v008a019>

10 Appendix

Table 4 | Surface DSC on TCIA data set

Organ	M/H	TCIA test set patient ID																				mean, stddev	diff.					
		0522c_0017	0522c_0057	0522c_0161	0522c_0226	0522c_0248	0522c_0251	0522c_0331	0522c_0416	0522c_0419	0522c_0427	0522c_0457	0522c_0479	0522c_0629	0522c_0768	0522c_0770	0522c_0773	0522c_0845	TCGA-CV-7236	TCGA-CV-7243	TCGA-CV-7245	TCGA-CV-A6JO	TCGA-CV-A6JY	TCGA-CV-A6K0	TCGA-CV-A6K1			
Brain (84056.5 mm ²)	(M)	93.7	94.2	96.3	94.5	93.7	92.7	93.3	98.3	93.5	92.9	97.1	94.6	95.1	97.3	94.2	94.5	96.9	97.2	97.0	94.6	96.1	96.1	95.4	94.4	95.1±1.5	-1.1	
	(H)	96.9	95.8	96.5	94.7	93.4	96.5	96.0	96.8	94.7	96.0	98.0	95.8	96.9	98.2	96.1	97.3	96.7	97.6	95.7	96.5	97.2	95.6	95.3	95.3	96.2±1.1		
Brainstem (6580.3 mm ²)	(M)	80.3	67.1	93.0	76.9	59.9	72.0	66.3	98.7	84.0	65.4	97.6	76.5	96.4	94.4	62.9	56.4	96.0	98.7	95.4	92.9	90.7	90.7	86.9	93.7	83.0±13.7	-13.7	
	(H)	96.3	96.9	88.5	95.9	93.0	99.2	94.0	97.3	97.3	92.6	99.6	95.9	97.4	99.6	96.6	97.1	98.5	98.0	97.8	97.5	99.0	98.0	97.8	97.7	96.7±2.5		
Cochlea-Lt (89.6 mm ²)	(M)	95.0	100.0	97.3	96.8	100.0	100.0	100.0	99.7	97.5	92.7	95.8	100.0	100.0	100.0	95.0	100.0	100.0	100.0	100.0	100.0	98.3	100.0	97.9	100.0	98.6	98.6±2.1	2.2
	(H)	100.0	100.0	89.7	93.5	94.3	90.5	100.0	90.0	100.0	94.5	100.0	99.2	94.3	100.0	98.7	100.0	92.2	92.8	91.0	100.0	100.0	99.6	91.6	100.0	96.3±4.0		
Cochlea-Rt (84.1 mm ²)	(M)	100.0	98.7	99.0	92.5	100.0	100.0	98.7	99.2	94.7	94.2	97.0	93.5	100.0	99.6	100.0	100.0	100.0	100.0	100.0	93.8	100.0	98.7	100.0	97.8	97.8±3.2	5.8	
	(H)	100.0	100.0	0.0	100.0	95.1	88.0	90.1	100.0	100.0	94.1	100.0	100.0	100.0	100.0	98.4	95.5	82.7	93.3	77.1	94.7	100.0	100.0	100.0	98.8	92.0±20.1		
Lacrimal-Lt (527.9 mm ²)	(M)	(95.8)	(92.2)	(96.5)	(88.5)	(73.4)	(84.7)	(94.0)	(95.4)	(81.9)	(76.3)	(97.1)	(81.9)	(93.5)	(96.2)	(85.6)	(96.3)	(96.2)	(97.8)	(98.4)	(99.6)	(97.2)	(99.3)	(96.1)	(98.6)	92.2±7.4	-1.7	
	(H)	(99.9)	(90.6)	(84.8)	(98.4)	(88.3)	(99.6)	(91.5)	(90.5)	(85.7)	(99.9)	(99.9)	(95.3)	(99.9)	(95.2)	(90.8)	(87.7)	(92.8)	(92.6)	(89.0)	(96.2)	(98.4)	(93.5)	(94.9)	(97.7)	93.9±4.7		
Lacrimal-Rt (555.3 mm ²)	(M)	(95.7)	(96.2)	(98.3)	(83.8)	(82.6)	(86.3)	(86.3)	(86.5)	(96.0)	(69.9)	(91.4)	(89.0)	(91.7)	(96.9)	(88.1)	(78.7)	(88.4)	(96.1)	(99.2)	(97.2)	(89.2)	(96.9)	(92.1)	(94.8)	91.3±6.6	-1.7	
	(H)	(99.7)	(98.2)	(96.1)	(97.7)	(91.4)	(95.1)	(84.3)	(81.7)	(96.6)	(99.0)	(100.0)	(88.4)	(96.5)	(96.0)	(94.3)	(93.9)	(89.1)	(98.7)	(93.4)	(91.9)	(93.0)	(81.9)	(92.9)	(82.5)	93.0±5.5		
Lens-Lt (190.8 mm ²)	(M)	100.0	95.7	92.0	99.7	99.9	100.0	86.9	91.9	98.1	100.0	100.0	0.0	99.9	99.5	92.4	96.9	96.6	98.6	97.6	99.9	99.8	96.0	96.2	100.0	93.2±19.7	-4.9	
	(H)	100.0	96.1	100.0	95.0	99.9	100.0	100.0	100.0	95.6	99.9	100.0	88.5	100.0	99.9	95.9	97.4	94.7	100.0	97.6	99.9	99.4	96.5	100.0	99.4	98.2±2.7		
Lens-Rt (189.9 mm ²)	(M)	99.2	0.0	92.1	99.6	100.0	96.0	95.3	0.0	95.5	95.4	100.0	0.0	93.1	95.9	98.9	96.3	99.8	92.0	95.8	100.0	99.9	99.4	91.8	95.7	84.7±32.1	-11.6	
	(H)	100.0	74.1	96.9	99.9	100.0	96.2	95.7	81.0	99.4	100.0	100.0	85.1	99.8	96.1	100.0	97.5	100.0	92.8	96.0	99.7	100.0	99.2	100.0	100.0	96.2±6.6		
Lung-Lt (59476.5 mm ²)	(M)	(99.4)	(98.7)	(93.9)	(98.9)	(96.9)	(98.6)	(87.8)	(96.8)	(98.1)	(98.4)	(99.0)	(97.1)	(95.1)	(99.2)	(99.4)	(98.0)	(98.6)	(99.6)	(99.0)	(98.6)	(99.4)	(99.6)	(99.0)	(98.4)	97.8±2.5	-0.1	
	(H)	(98.8)	(99.3)	(99.8)	(97.1)	(97.1)	(96.0)	(96.9)	(95.2)	(99.1)	(98.5)	(100.0)	(97.5)	(97.5)	(99.1)	(97.7)	(97.5)	(98.2)	(99.0)	(99.4)	(98.8)	(99.2)	(96.4)	(99.9)	(90.7)	97.9±2.0		
Lung-Rt (61894.6 mm ²)	(M)	(99.2)	(98.7)	(80.3)	(98.6)	(98.1)	(98.7)	(90.7)	(93.9)	(98.2)	(98.7)	(98.3)	(96.2)	(92.2)	(98.7)	(99.1)	(95.3)	(99.2)	(98.7)	(99.2)	(98.4)	(98.5)	(99.5)	(99.5)	(97.0)	96.9±4.1	-1.3	
	(H)	(98.7)	(99.4)	(99.8)	(96.7)	(97.8)	(98.7)	(97.1)	(95.2)	(98.2)	(98.4)	(100.0)	(97.9)	(97.0)	(99.3)	(94.9)	(99.0)	(99.2)	(98.1)	(98.4)	(97.0)	(99.8)	(96.1)	98.1±1.4				
Mandible (20870.5 mm ²)	(M)	96.9	96.1	97.3	94.0	96.7	98.4	93.4	97.3	97.1	96.3	99.9	94.0	98.9	97.4	93.0	94.2	98.2	98.4	97.4	99.0	99.0	95.3	95.8	98.6	96.8±1.9	-1.2	
	(H)	99.0	99.9	96.1	97.3	99.5	94.3	97.7	99.5	95.8	99.3	100.0	99.4	99.8	98.9	99.5	93.6	92.4	98.5	96.7	98.1	98.8	99.2	99.4	98.3	98.0±2.1		
Optic-Nerve-Lt (712.6 mm ²)	(M)	95.4	98.9	98.5	99.7	95.5	93.4	97.8	93.2	90.5	99.4	99.2	100.0	94.8	99.3	98.8	99.9	97.7	99.6	100.0	98.9	99.9	98.9	98.4	94.5	97.6±2.6	1.6	
	(H)	88.9	99.3	99.8	99.2	91.5	98.6	99.3	94.9	85.7	90.3	98.3	98.7	95.9	96.4	91.1	100.0	99.9	100.0	100.0	91.7	94.7	96.3	98.4	95.4	96.0±4.0		
Optic-Nerve-Rt (701.7 mm ²)	(M)	92.7	98.6	98.7	99.8	98.7	96.3	98.1	99.1	99.8	99.9	97.1	93.5	89.7	99.7	100.0	99.3	94.9	93.8	96.3	97.2	99.7	100.0	99.7	90.8	97.2±3.0	0.3	
	(H)	88.0	99.3	95.1	96.8	94.6	99.7	98.5	98.7	95.2	99.8	99.3	99.5	99.5	94.5	98.5	96.6	100.0	99.5	99.7	95.0	93.2	96.2	95.3	97.7	96.2	97.0±2.8	
Orbit-Lt (2307.9 mm ²)	(M)	94.7	95.8	91.4	94.6	94.6	88.6	91.9	94.6	95.7	98.6	98.5	94.3	98.1	91.7	93.3	83.1	97.9	92.6	87.6	90.3	94.7	91.9	90.4	97.8	93.4±3.7	-2.0	
	(H)	97.3	98.2	95.2	92.4	93.7	92.8	95.2	96.4	98.2	95.5	98.0	98.6	98.3	97.2	97.9	89.8	99.7	93.6	89.2	88.9	99.4	96.1	93.5	96.0	95.5±3.1		
Orbit-Rt (2355.7 mm ²)	(M)	96.8	97.4	92.5	96.9	97.2	91.7	92.7	91.2	98.6	99.3	96.6	94.7	95.9	93.0	95.7	85.3	99.3	92.0	93.1	96.4	90.4	90.9	96.8	93.0	94.5±3.3	-0.7	
	(H)	99.5	93.9	92.5	95.5	98.1	95.3	97.6	97.1	95.2	97.4	96.1	92.7	99.9	94.7	95.4	90.9	95.6	92.9	96.7	89.1	99.1	91.0	96.0	90.9	95.1±2.9		
Parotid-Lt (7978.0 mm ²)	(M)	91.6	79.4	90.2	93.8	91.2	94.4	68.4	95.6	75.6	88.9	92.8	91.1	95.4	97.5	84.5	87.2	94.3	92.3	92.8	92.4	84.8	74.6	94.8	97.9	89.2±7.5	-4.8	
	(H)	93.7	81.8	92.7	93.7	96.0	98.0	87.8	91.3	99.0	96.0	97.9	92.8	97.1	97.4	99.0	89.2	90.3	92.7	97.0	93.6	97.2	89.5	96.6	97.2	94.1±4.1		
Parotid-Rt (8307.5 mm ²)	(M)	95.2	81.8	88.0	93.4	95.8	83.3	91.3	91.6	72.9	91.5	97.1	91.9	93.3	96.1	86.2	92.3	88.7	91.6	94.2	93.7	73.2	94.0	90.4	93.9	90.1±6.3	-4.3	
	(H)	96.1	89.9	90.5	89.3	97.5	94.7	92.6	97.7	92.5	94.8	99.4	98.7	92.8	96.8	94.2	95.2	94.8	93.7	97.1	92.2	92.5	97.2	89.7	94.6	94.4±2.8		
Spinal-Canal (18278.6 mm ²)	(M)	(96.2)	(92.1)	(97.9)	(93.0)	(92.0)	(90.8)	(87.9)	(95.3)	(87.5)	(88.8)	(96.5)	(92.8)	(90.0)	(91.6)	(86.6)	(97.6)	(88.2)	(94.4)	(91.9)	(93.6)	(98.2)	(94.8)	(92.4)	(92.3)	92.6±3.3	-2.3	
	(H)	(95.2)	(96.2)	(95.7)	(91.1)	(94.4)	(92.3)	(95.7)	(94.7)	(96.0)	(97.1)	(99.4)	(94.0)	(94.7)	(94.8)	(96.6)	(97.8)	(92.7)	(97.2)	(95.3)	(92.9)	(92.9)	(94.2)	(95.7)	(91.9)	94.9±1.9		
Spinal-Cord (8679.2 mm ²)	(M)	99.9	99.1	99.2	99.4	100.0	99.8	99.6	99.6	94.4	97.5	100.0	98.8	97.9	98.6	98.8	100.0	100.0	99.7	100.0	99.2	99.8	100.0	98.4	99.6	99.1±1.2	-0.6	
	(H)	99.1	9																									

Table 5 | Volumetric DSC on TCIA data set

		TCIA test set patient ID																													
Organ	M/H	0522c-0017	0522c-0057	0522c-0161	0522c-0226	0522c-0248	0522c-0251	0522c-0331	0522c-0416	0522c-0419	0522c-0427	0522c-0457	0522c-0479	0522c-0629	0522c-0768	0522c-0770	TCGA-CV-7236	TCGA-CV-7243	TCGA-CV-7245	TCGA-CV-A6J0	TCGA-CV-A6JY	TCGA-CV-A8K0	TCGA-CV-A6K1	mean	stddev	diff.					
Brain (1382857.1 mm ³)	(M)	98.9	98.8	99.2	98.7	98.8	98.2	98.8	99.2	98.8	98.8	99.1	98.9	99.1	99.1	99.2	98.8	98.8	99.0	99.3	99.3	98.9	99.2	99.2	99.0	99.0	99.0±0.2	99.1±0.3	-0.1		
	(H)	99.2	99.1	99.3	98.7	98.7	98.9	98.9	98.7	98.8	99.2	99.8	99.1	99.1	99.3	99.3	99.1	99.1	98.9	99.3	99.1	99.1	99.3	98.6	98.9	99.0	99.0	99.0	99.1±0.3	99.1±0.3	-0.1
Brainstem (27219.8 mm ³)	(M)	78.0	69.2	82.9	73.2	67.6	70.1	71.4	90.8	78.1	63.6	91.2	69.6	89.1	88.9	66.0	59.3	86.9	87.4	87.1	85.5	82.6	86.3	86.0	87.9		79.1±9.6		-10.4		
	(H)	90.4	90.4	86.9	86.0	86.2	92.3	87.0	89.2	88.9	86.8	94.9	87.0	91.1	92.8	88.9	91.9	91.3	89.4	90.2	88.5	91.3	87.5	89.4	88.9		89.5±2.2		-10.4		
Cochlea-Lt (66.2 mm ³)	(M)	71.2	81.0	79.2	90.6	79.1	89.6	81.8	82.4	81.0	74.1	80.0	87.3	87.0	81.2	85.2	76.0	91.9	88.9	76.2	86.3	70.9	94.7	70.8	76.5		81.8±6.7		3.8		
	(H)	79.1	74.4	75.7	81.6	73.9	70.2	71.4	68.8	89.5	72.3	100.0	75.8	75.9	90.9	76.9	81.8	70.0	78.8	62.7	88.0	79.5	80.6	72.4	80.4		77.9±8.0		3.8		
Cochlea-Rt (63.9 mm ³)	(M)	83.0	85.7	90.3	83.6	86.4	89.6	77.6	82.8	71.7	77.3	68.8	80.0	82.5	83.9	83.3	86.8	78.8	81.0	55.9	89.8	71.6	90.9	80.0	77.8		80.8±7.8		8.8		
	(H)	71.4	92.3	0.0	81.8	61.8	60.4	51.3	86.7	97.4	76.2	100.0	83.7	72.5	88.0	73.7	61.9	55.0	66.7	51.7	72.7	93.3	72.7	84.2	72.5		72.0±20.3		8.8		
Lacrimal-Lt (585.6 mm ³)	(M)	62.0	60.8	75.9	56.4	37.6	51.8	48.9	69.3	51.9	37.8	72.4	36.7	68.3	66.5	44.4	68.8	66.2	70.8	71.1	80.4	73.9	77.6	68.5	66.3		61.8±12.9		-3.8		
	(H)	83.4	53.0	52.2	67.9	57.6	79.7	48.3	63.2	60.2	74.7	89.2	55.8	70.7	62.1	63.4	50.2	74.0	66.7	66.3	58.3	75.7	66.8	70.1	65.3		65.6±10.3		-3.8		
Lacrimal-Rt (629.8 mm ³)	(M)	56.8	60.8	79.9	48.2	44.2	54.4	44.8	51.0	64.5	37.0	62.7	50.4	62.7	68.1	55.2	69.8	62.0	69.0	80.6	65.3	58.8	72.7	64.9	70.4		60.6±10.8		-5.9		
	(H)	78.6	68.3	69.3	66.4	54.8	76.1	52.0	62.2	65.0	77.0	98.5	54.6	74.8	63.0	59.0	66.5	67.6	79.4	60.5	58.0	69.8	52.8	65.1	56.8		66.5±10.4		-5.9		
Lens-Lt (193.9 mm ³)	(M)	85.5	77.7	73.8	87.3	87.0	91.4	79.6	60.0	82.6	86.2	83.5	0.0	91.3	86.0	65.0	90.9	79.4	91.3	82.6	87.9	88.1	87.5	86.2	89.4		80.0±18.4		-7.2		
	(H)	89.8	81.0	95.6	88.7	94.1	90.9	89.9	88.2	84.1	80.3	100.0	54.1	93.0	86.0	86.5	87.4	80.0	93.9	86.8	88.2	90.1	87.4	89.3	88.1		87.2±8.3		-7.2		
Lens-Rt (194.3 mm ³)	(M)	82.2	0.0	66.7	81.7	86.7	85.5	81.1	0.0	84.7	83.3	87.0	0.0	78.4	82.2	76.9	81.6	91.4	76.6	84.4	92.1	91.8	88.6	80.4	90.5		73.1±28.2		-10.3		
	(H)	90.5	44.2	87.3	89.0	96.2	90.1	83.2	45.9	85.1	91.9	100.0	41.5	90.2	83.2	92.0	90.1	81.7	84.1	83.0	86.7	96.1	84.4	90.9	93.1		83.4±15.6		-10.3		
Lung-Lt (699853.3 mm ³)	(M)	99.2	98.9	98.4	99.3	98.7	98.8	97.0	98.6	99.0	99.1	98.5	99.1	97.0	99.1	99.3	98.7	98.4	99.2	99.1	99.3	98.9	99.3	98.7	99.1		98.8±0.6		0.1		
	(H)	99.1	99.2	99.1	98.2	98.5	98.0	98.2	97.5	99.1	99.1	100.0	99.0	97.8	98.8	99.0	98.1	98.4	99.1	99.3	99.2	99.0	98.0	99.4	96.9		98.7±0.7		0.1		
Lung-Rt (781938.8 mm ³)	(M)	99.3	98.9	94.9	99.2	98.9	99.1	97.8	98.2	98.7	99.2	98.6	98.9	96.7	99.2	99.4	98.5	98.5	99.1	99.2	99.3	98.8	99.3	98.8	98.6		98.6±1.0		-0.2		
	(H)	99.0	99.2	99.3	98.3	98.8	98.9	98.7	98.0	99.1	99.2	100.0	99.0	98.0	98.7	98.9	98.0	98.7	99.2	99.3	99.1	98.9	98.1	99.1	98.1		98.8±0.5		-0.2		
Mandible (58458.4 mm ³)	(M)	92.2	94.0	93.8	91.3	95.0	95.4	91.1	92.3	95.4	94.4	96.4	92.4	93.8	91.0	93.2	91.9	94.8	94.6	92.3	95.5	96.5	93.3	95.4	95.4		93.8±1.6		-0.1		
	(H)	95.6	97.1	92.6	94.1	94.3	90.1	91.6	94.6	92.5	94.7	100.0	95.6	94.2	92.0	95.1	90.0	90.4	95.5	95.4	91.6	93.9	95.3	94.2	93.6		93.9±2.3		-0.1		
Optic-Nerve-Lt (744.0 mm ³)	(M)	68.3	73.5	79.5	77.9	81.9	70.7	71.4	70.9	75.2	78.6	75.6	80.6	83.2	74.8	71.1	84.1	80.7	78.0	81.0	85.4	85.5	82.2	84.6	78.7		78.1±5.1		-0.7		
	(H)	67.0	80.4	75.8	79.7	74.2	88.9	80.3	75.2	76.7	70.9	82.6	82.6	80.6	79.2	69.5	82.7	83.3	82.7	81.2	77.8	81.2	83.8	81.4	73.3		78.8±5.0		-0.7		
Optic-Nerve-Rt (715.2 mm ³)	(M)	70.4	75.3	76.6	78.6	77.8	75.2	72.8	73.1	84.3	79.6	81.4	77.7	71.7	76.7	79.2	81.8	78.0	80.6	77.4	73.0	77.4	82.4	85.9	61.4		77.0±5.0		-0.6		
	(H)	73.0	81.7	76.7	73.9	68.8	81.7	75.0	69.4	76.7	76.9	97.0	81.2	75.9	73.3	66.7	78.3	87.0	80.6	69.7	76.0	80.3	80.9	84.2	77.7		77.6±6.4		-0.6		
Orbit-Lt (8408.1 mm ³)	(M)	90.1	92.1	91.1	91.2	92.7	89.4	92.3	90.5	92.6	93.8	94.3	93.4	94.5	88.1	91.7	84.4	93.2	92.1	90.4	90.6	92.6	91.4	90.9	93.1		91.5±2.1		-1.3		
	(H)	92.7	93.7	93.2	91.0	91.7	93.0	91.7	93.1	93.2	94.1	96.2	95.2	92.0	92.6	94.6	87.0	94.7	92.3	92.0	89.9	94.9	94.7	91.6	93.7		92.9±1.9		-1.3		
Orbit-Rt (8630.3 mm ³)	(M)	92.7	93.6	91.1	93.6	94.4	90.4	92.1	90.1	94.2	94.5	92.9	93.5	93.4	90.0	92.2	86.3	94.1	91.4	93.0	91.0	90.0	91.1	93.4	92.2		92.1±1.9		-0.8		
	(H)	95.2	92.2	91.2	93.3	94.0	93.0	93.3	94.4	93.4	95.5	95.3	91.1	94.9	91.8	94.0	88.3	93.2	92.2	93.7	90.1	94.1	92.9	92.8	91.7		93.0±1.7		-0.8		
Parotid-Lt (30036.5 mm ³)	(M)	81.0	78.6	81.2	86.4	80.8	86.4	66.8	87.6	72.2	85.8	86.3	83.2	85.8	87.2	83.8	82.1	87.2	82.8	88.9	86.5	82.2	75.3	89.7	89.0		83.2±5.4		-3.5		
	(H)	82.9	79.5	83.0	86.3	85.7	90.0	83.8	85.1	89.6	90.0	95.5	83.4	87.5	87.7	91.2	84.6	85.5	83.8	89.7	86.6	89.3	83.0	89.9	88.3		86.7±3.5		-3.5		
Parotid-Rt (31394.0 mm ³)	(M)	84.4	80.2	83.6	88.6	87.0	79.6	82.1	86.4	72.6	86.4	91.4	84.2	85.4	86.7	82.9	85.9	82.6	84.2	84.6	84.4	77.5	84.7	86.2	85.1		84.0±3.7		-2.9		
	(H)	84.3	85.0	86.1	84.8	88.5	87.5	83.0	90.2	85.2	89.1	98.3	87.8	82.3	87.6	89.2	88.4	87.3	84.6	88.5	83.8	87.6	86.1	85.4	86.1		87.0±3.1		-2.9		
Spinal-Canal (64045.2 mm ³)	(M)	94.6	91.5	95.3	93.4	92.6	92.3	91.2	93.2	89.2	89.8	92.7	93.2	91.6	91.2	89.0	95.2	89.9	93.2	93.0	90.9	96.0	92.8	91.4	92.8		92.3±1.8		-1.6		
	(H)	93.0	95.5	93.8	92.3	94.1	93.4	95.1	89.9	93.7	94.6	99.5	94.4	93.0	94.1	95.0	94.3	92.3	95.9	95.5	90.9	93.7	92.0	95.3	92.3		93.9±1.9		-1.6		
Spinal-Cord (18946.8 mm ³)	(M)	76.6	84.4	66.0	86.2	86.5	82.4	85.1	84.5	56.3	78.1	89.9	76.7	86.3	79.8	81.8	88.6	86.9	68.0	81.0	70.1	78.7	83.6	83.8	79.1		80.0±7.8		-4.0		
	(H)	81.0	86.2	75.3	85.2	86.9	84.8	85.0	83.4	70.0	83.2	92.2	82.8	84.7	80.1	86.9	89.9	88.2	79.4	85.3	77.9	85.1	87.9	87.2	87.8		84.0±4.8		-4.0		
Submandibular-Lt (9084.9 mm ³)	(M)	71.1	75.8	74.0	82.3	91.7	86.3	65.1	86.7	91.8	78.8	88.2	79.7	82.0	87.9	66.3	86.5	80.4	-	85.8	69.6	-	-	81.9	73.5		80.3±7.8		-3.1		
	(H)	81.5	90.7	88.5	85.8	90.7	88.6	73.7	89.7	92.6	91.0	99.8	83.0	90.1	91.5	88.1	94.3	69.8	-	90.1	0.0	-	-	85.3	84.8		83.3±19.7		-3.1		
Submandibular-Rt (9177.9 mm ³)	(M)	73.7	82.6	60.7	75.5	84.4	86.2	81.4	85.8	89.9	86.2	89.2	84.8	86.3	86.3	76.8	80.8	87.7	22.0	39.8	76.1	-	76.5	-	59.7	76.0±16.5		1.1			
	(H)																														

Numbers below the organ name show the average volume of this organ in the test set.

Numbers below the organ M: our model performance

H: human (radiographer) performance

Colors indicate performance differences: green: model is better, red: model is worse

Table 6 | Surface DSC on PDDCA data set

Organ	PDDCA test set patient ID														mean, stddev	
	off-site test set							on-site test set								
	0522c 0555	0522c 0576	0522c 0598	0522c 0659	0522c 0661	0522c 0687	0522c 0689	0522c 0708	0522c 0727 c	0522c 0746	0522c 0788	0522c 0806	0522c 0845	0522c 0857	0522c 0878	
Brainstem (5860.8 mm ²)	77.6	71.9	85.0	94.1	92.7	77.2	97.7	96.9	87.0	62.1	93.1	85.3	85.5	92.6	48.9	83.2±13.3
Mandible (19944.4 mm ²)	97.1	99.0	97.9	98.1	96.3	99.5	98.1	99.8	97.3	96.9	96.6	97.9	97.8	89.0	96.2	97.2±2.4
Optic-Nerve-Lt (619.1 mm ²)	96.7	94.1	96.0	88.2	86.9	93.1	97.4	85.9	91.1	85.5	99.7	81.5	98.3	98.7	90.5	92.3±5.5
Optic-Nerve-Rt (561.9 mm ²)	95.5	97.6	97.9	91.7	84.7	89.4	95.4	93.3	97.8	75.9	99.9	79.1	95.0	98.8	89.7	92.1±7.0
Parotid-Lt (7802.2 mm ²)	94.3	93.0	97.8	92.1	96.9	94.2	96.0	98.9	88.7	88.7	97.7	90.3	96.0	96.7	95.9	94.5±3.2
Parotid-Rt (7712.2 mm ²)	88.8	95.9	98.6	92.1	98.0	96.1	96.3	94.5	92.4	64.6	98.7	86.7	94.7	96.1	80.0	91.6±8.7
Submandibular-Lt (2632.6 mm ²)	67.1	67.0	90.3	78.4	81.9	67.4	87.9	81.0	95.8	68.1	98.5	75.9	72.1	98.5	79.8	80.7±11.0
Submandibular-Rt (2665.0 mm ²)	74.3	72.4	94.0	83.3	81.7	92.1	86.9	82.5	98.4	57.7	98.5	77.4	78.0	77.7	79.2	82.3±10.4
aggr. surface dice	90.7	89.9	95.7	93.5	94.1	92.3	96.4	95.9	93.8	80.4	96.9	90.5	92.9	92.1	85.9	

Numbers below the organ name show the average surface area of this organ in the PDDCA test set.

Table 7 | Volumetric DSC on PDDCA data set

Organ	PDDCA test set patient ID														mean, stddev	
	off-site test set							on-site test set								
	0522c 0555	0522c 0576	0522c 0598	0522c 0659	0522c 0661	0522c 0687	0522c 0689	0522c 0708	0522c 0727 c	0522c 0746	0522c 0788	0522c 0806	0522c 0845	0522c 0857	0522c 0878	
Brainstem (25037.2 mm ³)	79.2	73.3	83.0	84.8	85.1	77.4	87.9	89.8	77.0	68.2	82.3	73.5	85.8	85.6	60.0	79.5±7.8
Mandible (56364.2 mm ³)	94.7	92.9	96.0	95.8	90.5	95.7	95.6	96.5	95.5	94.8	93.1	93.1	92.9	89.7	93.1	94.0±2.0
Optic-Nerve-Lt (568.3 mm ³)	70.6	78.2	70.8	69.8	63.7	72.1	79.6	66.4	67.7	64.4	75.0	62.5	74.8	81.0	77.9	71.6±5.8
Optic-Nerve-Rt (482.2 mm ³)	70.8	74.8	77.3	63.3	61.0	62.7	64.2	72.3	79.6	60.4	77.0	61.1	66.2	80.8	73.3	69.7±7.1
Parotid-Lt (30356.3 mm ³)	86.2	86.3	89.9	81.3	90.4	89.0	88.1	89.2	83.2	81.9	88.4	83.5	88.4	88.6	86.1	86.7±2.8
Parotid-Rt (30396.0 mm ³)	84.4	88.7	91.3	83.6	90.1	89.8	86.1	87.2	85.8	64.9	89.2	83.2	86.9	88.3	79.9	85.3±6.2
Submandibular-Lt (7091.3 mm ³)	67.8	62.8	82.9	74.2	79.7	67.0	78.9	78.5	86.1	64.5	90.4	73.0	65.1	90.4	78.4	76.0±8.9
Submandibular-Rt (7195.0 mm ³)	77.1	73.4	84.0	76.1	76.3	86.1	82.7	76.8	88.7	60.4	90.4	77.8	75.9	71.6	70.6	77.9±7.4

Numbers below the organ name show the average volume of this organ in the PDDCA test set.

Table 8 | Number of labelled scans in UCLH test set

	Brain	Brainstem	Cochlea	Lacrimal	Lens	Lung	Mandible	Optic Nerve	Orbit	Parotid	Spinal-Canal	Spinal-Cord	Submandibular			
			lt	rt	lt	rt	lt	rt	lt	rt	lt	rt	lt	rt		
Number of scans	75	45	8	8	75	73	75	73	71	72	74	17	15	19	16	
Dense segmentation			✓	✓	✓	✓	✓	✓			✓	✓			33	32
Number of labelled slices	axial	309	225			265	275	300			95	75	165	160	345	350
	coronal	374	225			355	360	375			95	80	165	160	0	0
	sagittal	374	225			355	360	375			95	80	165	160	0	0
															23	24
															64	65

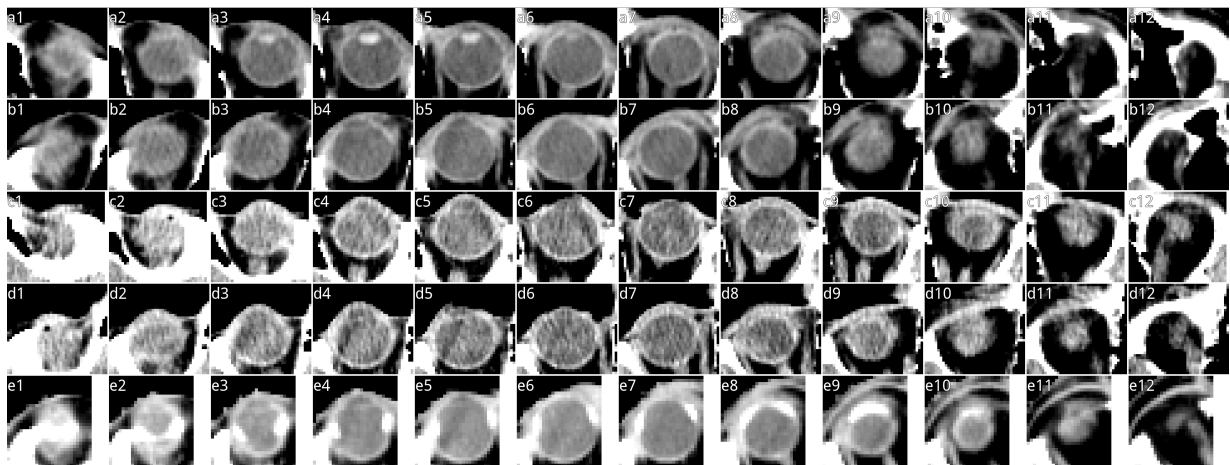


Figure 10 | Missed lens predictions across the TCIA test set. Consecutive axial slices of eyes showing both a typical lens and the four cases where the model predictions omitted the lens. The window level is at a constant W:140 L:0. **(a1-a12)** 12 slices through a single eye in which the model was able to detect the lens, which is clearly visible in (a3-a6). (a1) is the upper most slice, (a12) the lower most. **(b1-e12)** Similar to the first row, but these four cases are those for which the model was unable to differentiate the lens from the rest of the eye. Note that all four cases are considerably more challenging than for the first row.

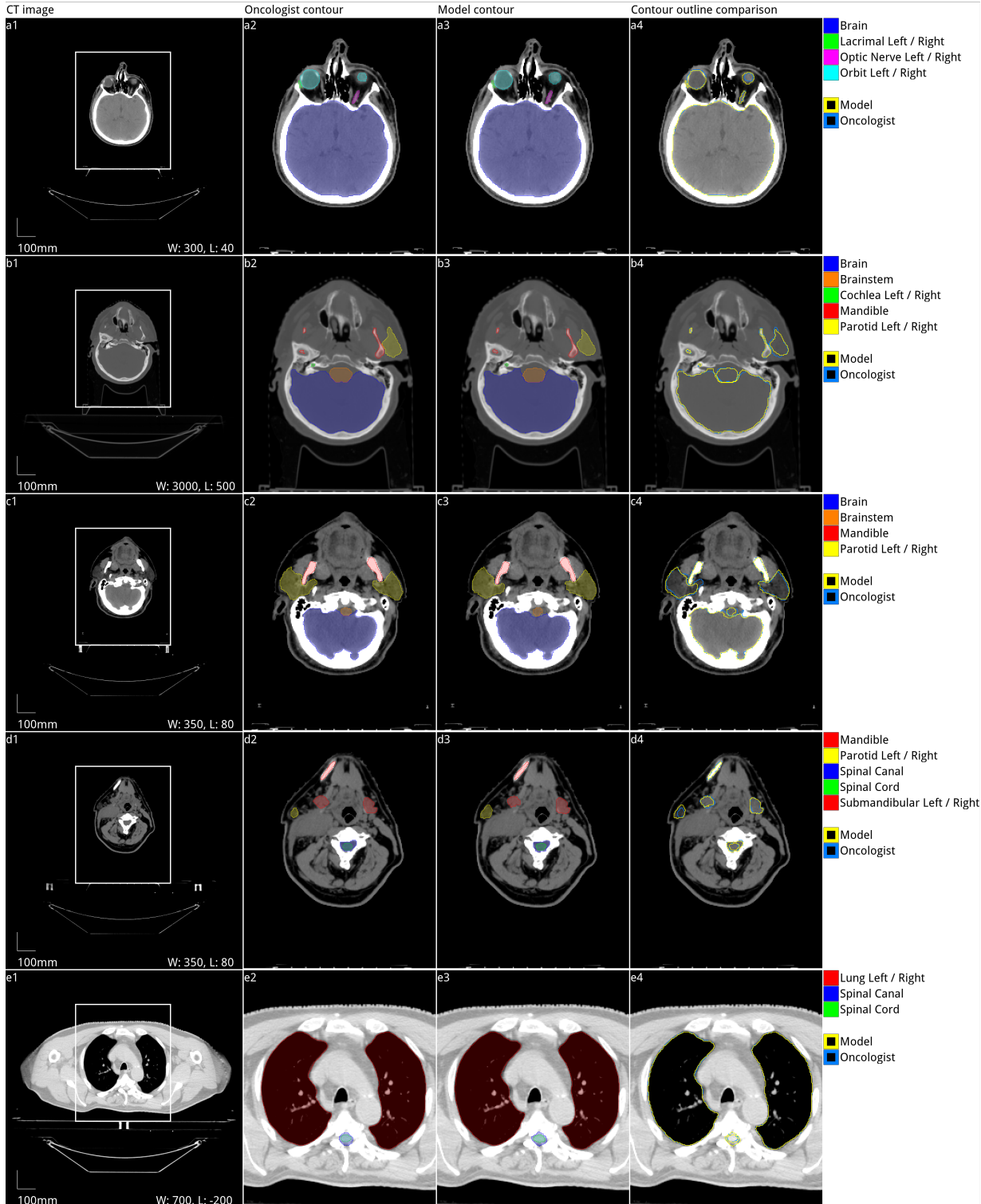


Figure 11 | Example results from a second randomly selected case from the TCIA test set. Five axial slices from the scan of a 58 year old male patient with a cancer of the right tonsil selected from the Head-Neck Cetuximab TCIA dataset (patient 0522c0416; [37]). (a1-e1) The raw CT scan slices at five representative levels were selected to best demonstrate the OARs included in the work. The window levelling has been adjusted for each to best display the anatomy present. (a2-e2) The ground truth segmentation was defined by experienced radiographers and arbitrated by a head and neck specialist oncologist. (a3-e3) The model produced segmentations of the same structures. Overlap between the model (yellow line) and the ground truth (blue line) is shown in (a4-e4). Best viewed on a display.

